

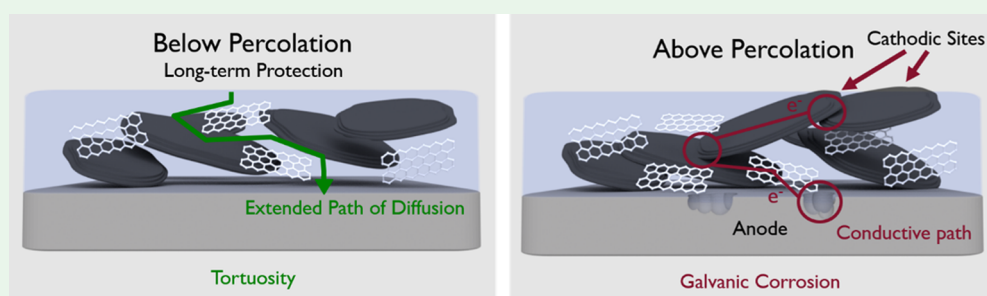
# Tortuosity but Not Percolation: Design of Exfoliated Graphite Nanocomposite Coatings for Extended Corrosion Protection of Aluminum Alloys

Rachel D. Davidson,<sup>†,‡,¶</sup> Yenny Cubides,<sup>‡,¶</sup> Cole Fincher,<sup>§</sup> Peter Stein,<sup>⊥</sup> Chelsea McLain,<sup>†</sup> Bai-Xiang Xu,<sup>⊥</sup> Matt Pharr,<sup>§</sup> Homero Castaneda,<sup>\*,‡</sup> and Sarbajit Banerjee<sup>\*,†,‡</sup>

<sup>†</sup>Department of Chemistry, <sup>‡</sup>Department of Materials Science & Engineering, and <sup>§</sup>Department of Mechanical Engineering, Texas A&M University, College Station, Texas 77843, United States

<sup>⊥</sup>Mechanics of Functional Materials Division, Department of Materials and Earth Sciences, Technische Universität Darmstadt, Jovanka-Bontschits-Str. 2, 64287 Darmstadt, Germany

## Supporting Information



**ABSTRACT:** Increased adoption of engineered aluminum alloys in vehicular components is imperative for automotive lightweighting, but such alloys are oftentimes prone to degradation upon exposure to corrosive environments. The design of coatings to inhibit corrosion of aluminum alloys has emerged as a critical need but given the electropositive nature of the substrates, only a sparse few options are available. In this article, we explore the corrosion resistance afforded to aluminum alloy AA7075 substrates by unfunctionalized exfoliated graphite nanocomposite coatings as a function of the exfoliated graphite loading. Detailed mechanistic understanding is developed through monitoring progression of the open circuit potential and electrochemical impedance response of the substrates over 100 days of immersion in a saline environment along with post-mortem cross-sectional scanning electron microscopy and energy dispersive X-ray spectroscopy analysis of sectioned interfaces. Electrochemical studies along with nanoindentation, AC conductivity measurements, and salt spray exposure studies allow for a direct evaluation of the role of exfoliated graphite in inhibiting/accelerating corrosion. Indeed, we identify two distinctive regimes: excellent long-term corrosion resistance is obtained at low exfoliated graphite loadings within a polyetherimide matrix as a result of a substantial enhancement in the tortuosity of ion transport pathways for diffusion of corrosive species; however, further inclusion of exfoliated graphite results in formation of a percolative network that gives rise to accelerated galvanic corrosion of the underlying substrate. Finite element modeling shows that a broad distribution of particle sizes of graphene inclusions is particularly favorable for enhancing tortuosity. Cross-sectional scanning electron microscopy analysis of a 5 wt % exfoliated graphite nanocomposite coating after salt water exposure for 100 days indicates complete retention of coating integrity and an uncompromised interface with the metal surface, which is in stark comparison to the bare polyetherimide matrix, which is plagued by extensive delamination and shows significant interfacial accumulation of corrosion products. Higher graphene loadings beyond the percolation threshold show evidence for severe galvanic corrosion with corrosion products distributed along the thickness of the coating. The results provide evidence that exfoliated graphite can offer performance that is equivalent to that of pristine and functionalized graphene in terms of inhibiting corrosion and suggest an approach for enhancing barrier protection through increased resistance to pore transport enabled by the excellent dispersion of exfoliated graphite sheets within polymeric matrices.

**KEYWORDS:** *graphite, corrosion, percolation, galvanic corrosion, tortuosity, exfoliated graphite*

## INTRODUCTION

The strong impetus for reducing fuel consumption along with increasingly stringent global emissions standards has spurred a worldwide push toward lightweighting of vehicles.<sup>1–5</sup> Light-

**Received:** March 9, 2019

**Accepted:** May 2, 2019

**Published:** May 2, 2019

weighting of vehicular components is most often targeted through (a) the replacement of steel by magnesium and aluminum alloys, engineered polymers, or carbon fiber composites or (b) the design of porous monolithic forms (increasingly accessible from additive manufacturing methods) that provide load-bearing capabilities and mechanical resilience comparable to fully dense fabricated parts but with much greater economy of material consumption.<sup>6,7</sup> In contrast to vehicular transportation, the use of lightweight metal alloys is much more prevalent in other sectors where they are designed to meet demanding structural specifications. For instance, high-strength aluminum alloys have served for over 80 years as the primary structural material used in aircraft construction.<sup>8</sup> While aluminum metal itself is prone to corrosion at low and high pH values, the addition of other metals, as required to stabilize high-strength alloys, further exacerbates this problem by giving rise to a complex microstructure with a diverse range of intermetallic inclusions and precipitates that render the resulting alloy vulnerable to local corrosion. Indeed, corrosion cells are readily established across the surface of a heterogeneous alloy upon exposure to an electrolyte environment. Failure of vehicular structural components because of corrosion can give rise to serious passenger safety issues. The need to replace failing parts furthermore decreases service life and thereby increases the cradle-to-grave environmental impact of engineered alloys.<sup>2,3</sup> Chromium-based conversion coatings provide excellent corrosion protection of aluminum and have been the mainstay for corrosion protection in the aerospace industry; however, it is well established that hexavalent chromium effluents released at various points in the production, use, and as disposal of such coatings are highly toxic as well as carcinogenic.<sup>9</sup> Indeed, concerns regarding the ecological toxicity and human health impact of hexavalent chrome have led to strict regulation of its use in commercial products.<sup>10,11</sup> With increasing use of aluminum alloys for vehicular applications, the development of sustainable chrome-free coatings has emerged as an urgent imperative. The  $-1.66$  V value of the  $\text{Al}^{3+}/\text{Al}$  redox couple (versus SHE) implies that zinc and trivalent chrome commonly used to protect steel substrates are ineffective at providing sacrificial cathodic protection to aluminum alloys. Magnesium-based nanocomposite coatings have instead been developed to provide sacrificial protection to aluminum alloy substrates and are effective under certain environments<sup>12–14</sup> but are plagued by issues such as the typically high reactivity of Mg particles, the complexity of preparing surface-passivated Mg pigments that can be safely handled, and the need for relatively thick coatings spanning scores of microns. In this article, we demonstrate an alternative approach wherein unfunctionalized exfoliated graphite (UFG) nanocomposite coatings with sub- $30\ \mu\text{m}$  thickness dispersed within a polyetherimide matrix show excellent corrosion inhibition of AA7075 substrates upon prolonged exposure to saline environments. A detailed mechanistic elucidation of the origins of corrosion protection afforded by such coatings has been performed using open circuit potential measurements, electrochemical impedance spectroscopy, salt spray exposure testing, and post-mortem analysis of interfacial layers between the coating and substrate. The measurements suggest the excellent ability of exfoliated graphite to enhance the resistance to transport of corrosive species through barrier protection and increased tortuosity but emphasize the need to prevent galvanic corrosion, which can

be activated when a percolative network of UFG is constituted within the polymeric matrix.

Graphene has received significant attention as a means of designing more sustainable coatings for corrosion inhibition. The efficacy and mechanism of corrosion inhibition provided by graphene remain somewhat controversial; the debate derives in part from the diversity of materials delineated as graphene coatings (ranging from monolayer graphene grown by chemical vapor deposition and transferred onto metal substrates to exfoliated graphene, graphene oxide dispersed within polymeric matrices and cast as nanocomposite coatings, electroplated graphene/metal thin films, and tubular graphene derived by Nguyen and co-workers through thermal annealing)<sup>15–17</sup> and the differences in their mode of interfacial interaction with the surfaces sought to be protected.<sup>11,18</sup> Notably, given challenges inherent to the industrial production of pinhole-free monolayer graphene, much of the literature has focused on related materials that are much more readily accessible. While the electronic structure and thus transport properties of such materials are strongly dependent on the layer thickness, the barrier protection derived from ion-impermeable 2D sheets is anticipated to be largely preserved even for functionalized derivatives and thicker platelets that are not monolayer graphene.

Galvanic corrosion is a common mode of failure for graphene-based coatings. While the value of the electrode potential of graphene, or for that matter, graphite, varies as a function of the surface chemistry, the reported value of  $+0.150$  V reported for pure graphite versus SCE<sup>19</sup> is substantially higher as compared to pure aluminum ( $-0.76$  V versus SCE; corrosion potential of AA7075-T6 is  $-0.765$  V versus SCE);<sup>20</sup> consequently, galvanic corrosion of the latter is possible upon direct coupling.<sup>21</sup> Zettl and co-workers have shown that the corrosion of Cu is initially diminished by the presence of graphene layers deposited directly onto the substrates owing to the impermeability of graphene.<sup>22</sup> However, in the presence of defects, the permeated electrolyte establishes a corrosion cell between the graphene layer and the underlying copper substrate, which brings about accelerated galvanic corrosion of the underlying metal. Recent studies indicate that the accumulation of chloride ions at the edges of graphene facilitates metal oxidation and dissolution.<sup>23</sup> However, this picture is complicated by the strong interfacial hybridization of graphene to several transition metals, which results in substantial charge transfer and can give rise to potential barriers at the interface that can endow corrosion protection.<sup>24–26</sup> An alternative strand of research has focused on the corrosion protection endowed by graphene nanocomposites wherein few-layered chemically derived graphene flakes are embedded within a polymeric coating. As an impermeable 2D material,<sup>27</sup> inclusion of graphene adds substantial tortuosity to pathways for diffusion of species participating in the redox reactions of corrosion. Functionalization of graphene or incorporation of graphene in nonconductive polymers results in a considerable enhancement of the tortuosity of ion diffusion pathways and a substantially increased pore transport resistance while preventing direct electrochemical coupling with the substrate.<sup>28–33</sup>

The utilization of graphene as a filler within a polymeric system necessitates its effective dispersion within the host matrix, which can be achieved through surface functionalization, selection of a compatible polymer, achieving high loadings in solvents prior to mixing, or application of shear

forces.<sup>11,34</sup> Graphene has a tendency to agglomerate and restack within composites when chemical compatibility is poor; the resulting larger agglomerations form phase segregated domains that are much less effective at increasing the tortuosity of pathways for ion transport.<sup>35</sup> Achieving higher loadings of graphene in coatings is potentially beneficial for corrosion protection provided that electrochemical coupling resulting in galvanic corrosion can be avoided. Yang and co-workers have shown improved corrosion inhibition performance with higher loadings of graphene, which is attributed in part to the greater tendency of graphene to align at higher loadings, which extends the effective diffusion path that needs to be traversed by corrosive species from the surface to the substrate.<sup>36</sup> In addition to dispersibility at high loadings, several studies of graphene nanocomposite coatings have shown a dependence of functional performance on graphene flake size,<sup>37</sup> positioning within the polymer,<sup>38,39</sup> and the use of high-surface-area “crumpled” graphene.<sup>40</sup>

With a view toward the stabilization of few-layered nanosheets that can enhance the tortuosity of ion diffusion pathways, we eschew harsh oxidation methods that can introduce vacancies and holes and instead utilize unfunctionalized exfoliated graphite (UFG) derived from nonoxidative methods as our filler material. While characterized by a wide size distribution of layer thicknesses, unfunctionalized exfoliated graphite represents perhaps the most facile route to an industrially viable graphitic coating for corrosion inhibition given its ease of preparation and retention of crystallinity. Specifically, solvent-assisted exfoliation of graphite allows for retention of the conjugated  $\pi$ -framework without creation of porosity, thereby enabling  $\pi$ – $\pi$  interactions with the host polymeric matrix to be utilized to achieve effective dispersion at high loadings. In previous work, we have shown the remarkable corrosion resistance afforded by UFG/polyetherimide (PEI) composites for the protection of mild steel.<sup>11,36</sup> UFG is incorporated *in situ* during the ring-opening polymerization of the anhydride with two different amines to form polyamic acid; subsequently, polyamic acid is imidized to form PEI by thermal annealing after casting the films onto the metal substrates. The nanocomposite coatings show excellent corrosion performance based on Tafel analysis and extended exposure testing.<sup>13,41</sup> A life cycle assessment independently performed by Koratkar and co-workers has indicated that these coatings have a substantially lower cradle-to-grave environmental impact as compared to hot-dipped galvanized steel.<sup>37</sup>

In this article, we examine the corrosion protection afforded to aluminum alloy AA7075 substrates by UFG/PEI nanocomposites as a function of the exfoliated graphite loading. A detailed mechanistic study based on extensive electrochemical characterization allows for two distinct regimes to be distinguished. Excellent corrosion protection, which is competitive with or superior to graphene-based coatings, is obtained at relatively low loadings of UFG, but higher UFG loadings result in establishment of a percolative network that promotes galvanic corrosion. The electrochemical impedance response of the coatings immersed in salt water is monitored for 100 days yielding unprecedented mechanistic insight into the origins of the corrosion protection derived from the nanocomposite coatings. Consequently, these studies indicate that effective coatings must provide extensive tortuosity of diffusion paths for ionic species but ensure that an extended percolative network is not stabilized across extended length scales.

## ■ MATERIALS AND METHODS

**Synthesis of UFG.** UFG was prepared by exfoliation of graphite in *N*-methyl-2-pyrrolidone (NMP, Honeywell Research Chemicals).<sup>36</sup> To prepare different loadings of UFG dispersions, 5, 10, and 20 mg/mL of graphite (Bay carbon, SP-1 graphite powder) was ultrasonicated for 6 h and shaken every hour to avoid settling of larger unexfoliated graphite particles. The prepared UFG was examined by Raman spectroscopy and scanning electron microscopy (SEM). Size distribution statistics were obtained through combined atomic force microscopy (AFM) and SEM analysis. Given the large distribution of sizes obtained from the exfoliation process, the dimensions of larger particles on the order of tens of micrometers in width and  $2.5 \pm 2.1$   $\mu\text{m}$  thick and smaller particles on the order of a few hundred nanometers wide and 9–16 nm thick were analyzed separately, and statistics on the estimated proportions of large and small particles were additionally provided. Distributions of lateral dimensions of large and small particles were obtained with the help of the ImageJ-plugin analyzing numerous SEM images at different magnifications. An image contrast threshold was defined, and the dimensions of the larger particles were estimated with the help of Image-J. Thicknesses of larger particles were determined from cross-sectional imaging of the particles in SEM; thicknesses of smaller particles were evaluated by AFM using a Bruker Dimension Icon AFM. Gwyddion software was used for image analysis.

**Preparation of UFG/Polyamic Acid Dispersions.** Polyamic acid was prepared by the polymerization of 3,3',4,4'-biphenyl-tetracarboxylic dianhydride with 2,2'-(ethylenedioxy)bis(ethylamine) and *m*-phenylenediamine in NMP. In brief, the two diamines dissolved in NMP were heated to 70 °C under a stream of nitrogen within a round-bottom flask. The dianhydride was slowly added over the course of 5 min with rapid stirring. The resulting clear, yellow solution was further stirred under a stream of nitrogen for 8 h. To prepare UFG/PEI dispersions, the two diamines were added to UFG dispersions in NMP, followed by addition of the dianhydride as noted above.<sup>13,42</sup> Where required, additional UFG solution was added postsynthesis to achieve the intended UFG/polymer loadings.

**AA7075 Substrate and Surface Preparation.** Clad AA7075-T6 substrates were obtained from Aerotech Alloys. The nominal composition of AA7075-T6 is listed in Table S1. Prior to application of the coatings, the AA7075 substrates were abraded with P150 and P400 grit sand paper and washed with hexanes followed by acetone.

**UFG/PEI Coatings.** The UFG/polyamic acid dispersions were spray coated onto the cleaned AA7075 substrates using a TCP Global spray gun with an output pressure of 45 psi and a nozzle diameter of 1.00 mm. Substrates were held at a temperature of 250 °C during application of the coating and were subsequently cured for an additional 5 min. The thickness of the coatings was monitored using a Byko-test 8500 thickness gauge. All coatings were applied at a thickness of 20–30  $\mu\text{m}$ .

**Optical Microscopy and Raman Spectroscopy.** Raman spectra were acquired using a Jobin-Yvon Horiba Labram HR instrument coupled with an Olympus BX41 optical microscope. A 514.5 nm Ar-ion laser was used as the excitation source. Each of the prepared exfoliated graphite solutions was drop cast onto heated silicon substrates for analysis. Optical images were acquired using the Olympus BX41 optical microscope.

**AC Conductivity Measurements.** AC conductivity measurements were performed using a Gamry potentiostat/galvanostat/ZRA Reference 1000TM in the frequency range from 100 kHz to 10 mHz at an amplitude of 10 mV. The samples were sandwiched between two circular stainless steel electrodes, and the entire cell configuration was tightened with a screw. All samples were tested under dry conditions at room temperature. Coatings were measured as prepared, while UFG was analyzed by creating films drop cast onto AA7075 substrates.

**Adhesion Testing.** Adhesion testing was performed using three American Society for Testing of Materials (ASTM) standardized methods. As per ASTM D3359, a cross-cut test was performed using a test kit procured from BYK. Cross-cuts were made with 1 mm spacing

between blades, and the adhesive tape was subsequently applied and removed. A classification of 0–5B was assigned to each of the coatings tested as per the specifications of the testing protocol. A rating of 5B corresponded to no discernible removal of the coating, whereas a designation of 0B was reflective of significant damage. ASTM D4541–09 was used to evaluate the pull-off strength of the coatings. A 14 mm diameter dolly was applied to the surface of the coating using a two-part epoxy and allowed to cure for 24 h. The pucks were removed at a pull-off rate of 0.7 MPa/s using a PosiTect AT-A automatic adhesion tester manufactured by DeFelsko. ASTM D2197–16 was performed to evaluate scrape adhesion using a balance beam scrape adhesion tester. Samples were aligned under the scraping loop that supported the specified applied load. The samples were then slid along a linear path of 3 in. and monitored for damage. All adhesion testing was repeated in triplicate for each type of coating.

**Nanoindentation Experiments.** The elastic modulus and hardness of the films were measured using a Nanomechanics iMicro nanoindenter with an InForce 50 actuator and diamond Berkovich tip. Elastic analysis follows the procedure of Oliver—Pharr,<sup>43</sup> wherein the contact stiffness,  $S$ , was related to the elastic modulus,  $E$ , through the universal stiffness equation:

$$S = \beta \frac{2}{\sqrt{\pi}} E_r \sqrt{A} \quad (1)$$

where  $\beta$  is a geometric constant that depends on the indenter geometry (taken as 1 in this work), and  $A$  is the area of the elastic contact. Meanwhile,  $E_r$  is the effective modulus given as follows:

$$E_r = \left( \frac{1 - \nu_i}{E_i} + \frac{1 - \nu}{E} \right)^{-1} \quad (2)$$

where  $E_i$  and  $\nu_i$  represent the elastic modulus and Poisson's ratio of the indenter, whereas  $E$  and  $\nu$  represent the elastic modulus and Poisson's ratio of the indented sample. The hardness was estimated from the contact area as

$$H = \frac{P_{\max}}{A} \quad (3)$$

where  $P_{\max}$  is the peak indentation load. Both the frame stiffness and the depth–area relationship were empirically determined based upon the indentation response of a fused silica standard sample. Tests were conducted on each sample using a constant loading rate over a load setting of 0.05, 0.1, 0.2, and 0.3 s<sup>-1</sup>.

**Salt Spray Exposure.** Samples were exposed to salt spray conditions following procedures outlined in the ASTM B117 standard. The pressure of the chamber was kept at 15 psi. During exposure, the distribution of the spray was monitored using graduated cylinders distributed throughout the chamber. The collection volume for all cylinders was consistently between 20 and 50 mL per day. The back of the samples and edges were protected with tape to prevent preferential corrosion of uncoated sections. A 5 cm × 5 cm cross-sectional cut was made in each of the coatings using a diamond-tipped scribe. As specified in the standard, the samples were exposed to a spray generated from a 5 wt % aqueous solution of NaCl in a chamber held at 35 °C for the entirety of the testing cycle. Samples were monitored at 24 h intervals for 12 days.

**Electrochemical Impedance Spectroscopy (EIS).** EIS measurements were performed to characterize the electrochemical response and degradation of the different systems under consideration up to a period of 100 days in an aerated aqueous solution of 3.5 wt % NaCl at room temperature. The measurements were performed in a conventional three-electrode cell using the coated sample as the working electrode, a saturated calomel electrode (SCE) as the reference electrode, and a Pt/Nb mesh as the counter electrode. A cylindrical glass vessel was utilized as the electrochemical cell exposing an area of 4.67 cm<sup>2</sup> on the working electrode; an O-ring and a metallic clamp were used to hold together the working electrode and the glass vessel. Electrochemical data were collected using a Gamry potentiostat/galvanostat/ZRA Reference 1000TM instrument surrounded by a Faraday cage to minimize electromagnetic interference.

The open circuit potential (OCP) was measured for 10 min before each EIS measurement. The EIS measurements were carried out at the OCP in the frequency range of 100 kHz–10 mHz at 10 points per decade using a sinusoidal perturbation signal of ±10 mV. The electrochemical measurements were conducted on duplicate samples. The EIS spectra were fitted to appropriate equivalent circuit models using the EC-lab V10.40 fitting software.

**Cryo-Fracture, Cross-Sectional Analysis.** Coatings were cryo-fractured through immersion in liquid nitrogen for 5 min and then fractured and imaged using a JEOL JSM-7500F SEM without Pt coating to allow for localization of charging to be observed. The coatings were imaged at an accelerating voltage of 1 kV, an emission current of 10 μA, and a probe current of 8 μA.

**Transmission Electron Microscopy (TEM).** TEM was performed on a JEOL JEM-2010 instrument at an accelerating voltage of 200 kV. Prior to TEM measurements, a solution of the 10 wt % UFG/PEI polymer composite was drop-cast onto a Formvar-coated 400 mesh copper TEM grid that was heated to remove excess solvent.

**Cross-Sectional Analysis of Coating/Substrate Interface.** Cross-sections of a set of unexposed coatings as well as all those exposed for 100 days as part of the EIS study were prepared by immersing the coatings in epoxy (EpoxiCure 2, Buehler) and subsequently cutting the samples to expose the metal/coating interface using a Buehler Isomet 5000 system. The cross-sectional samples were sanded using 600, 1000, and 1200 grit paper and polished successively with 9, 6, and 1 μm diamond paste prior to imaging. The samples were subsequently sputtered with ~3 nm of Pt and imaged using a JEOL JSM-7500F SEM equipped with an Oxford Instruments energy dispersive X-ray spectroscopy (EDS) detector. EDS maps were obtained for each of the interfaces using an acceleration voltage of 10 kV, an emission current of 10 μA, and a probe current of 8 μA.

**Finite Element Modeling of Diffusivity.** A computational first-order homogenization scheme based on the Finite Element method was utilized to model effects of particle size distribution on effective diffusivity for composite coatings. Approximating the density of UFG by that of graphite,  $\rho = 2.2$  g/cm<sup>3</sup>, together with the density of PEI,  $\rho = 1.27$  g/cm<sup>3</sup>, the mass fractions of 5, 10, and 17 wt % were converted into corresponding volume fractions of 2.8, 5.4, 8.9 vol %, respectively. Using a random sequential addition algorithm, UFG flakes, represented by thin hexahedral slabs, within sample cells of dimensions 200 μm × 200 μm × 200 μm were placed within the matrix until reaching the desired volume fractions. Flake size distributions used in this approach are provided in Tables S2 and S3 (Supporting Information).

The effective diffusivity tensors were determined through solving a Laplace problem across the composite. For each of the three space directions, linear concentration/potential conditions have been prescribed on the sample surface. Effective diffusivity tensors can then be determined using the average flux vectors and concentration/voltage gradients in the specimen. To reduce the impact of the random microstructure, these calculations have been performed for five random samples each. The effective diffusivity then results from the trace of the average diffusivity tensor. For the diffusion calculations, we assumed the UFG to have a diffusivity near zero and assumed a unit diffusivity for the PEI matrix. The resulting effective diffusivity hence gave the relative change in diffusivity with respect to the diffusivity of the pristine PEI matrix.

## RESULTS AND DISCUSSION

**Characterization of UFG and UFG/PEI Nanocomposite Coatings on AA7075.** Challenges related to the dispersion of few-layered graphene at high loadings within solvents and polymeric matrices represent a significant constraint to the design of high-performance graphene inks and composites.<sup>34,44,45</sup> Exfoliation of unfunctionalized graphene monolayers in solution has been accomplished by Hernandez et al. but is limited to concentrations of ~1 wt % in

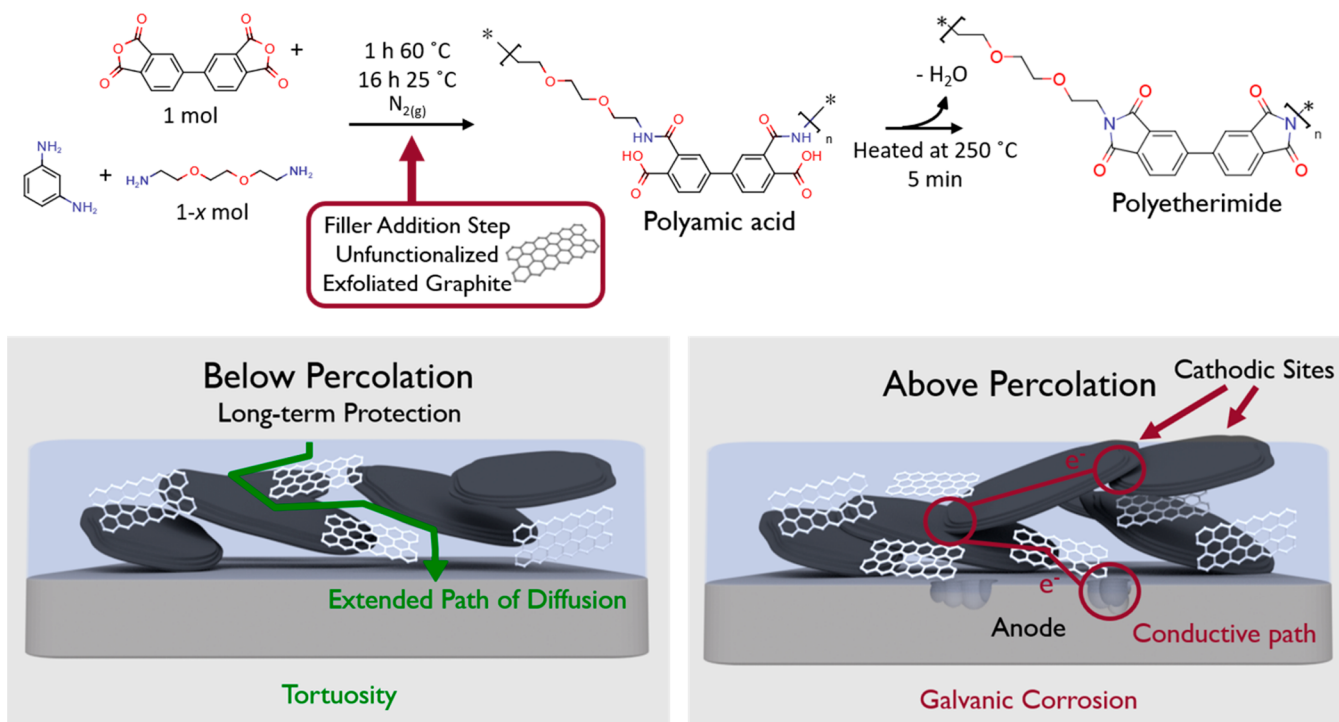


**Figure 1.** Schematic illustration of the preparation of nanocomposite exfoliated graphite coatings based on *in situ* synthesis of polyamic acid in the presence of UFG followed by imidization during curing. Two distinct regimes can be distinguished as a function of the UFG loading: (A) incorporation of UFG imbues considerable additional barrier protection at low loadings (of ca. 5 wt % UFG) as a result of increased tortuosity of ion transport pathways, whereas at higher loadings (ca. 10 wt % and higher), (B) galvanic corrosion is initiated owing to the coupling of the percolative UFG network with the underlying Al substrate.

NMP.<sup>46</sup> Exfoliated graphene prepared in this manner is characterized by extended  $\pi$ -conjugated domains without a high concentration of pores and damaged regions observed in graphene oxide.<sup>47</sup> Given that such pores in oxidatively functionalized graphene can potentially mediate undesirable ionic diffusion,<sup>48</sup> exfoliated UFG has been selected as the filler of choice for corrosion-resistant composites. Attempting to achieve higher-concentration UFG dispersions inevitably results in a greater abundance of thicker few-layered graphitic platelets. While the effective dispersion of individual sheets within the polymeric matrix is most desirable to maximize tortuosity, low-solid-content dispersions do not yield robust pinhole free coatings given the large solvent volume that must be removed during curing. Surfactants can be utilized to aid dispersibility at higher concentrations but often give rise to deleterious porosity. To balance the above constraints, extended ultrasonication has been used to obtain dispersions with relatively high loadings of 5, 10, and 20 mg/L of UFG without the addition of surfactants and without further fractionation, thereby yielding a mixture of larger few-layered platelets and thinner exfoliated flakes. This method allows for inclusion of a substantial proportion of exfoliated few-layered nanosheets enabling high-solid-loading dispersions in NMP while inevitably yielding a proportion of larger graphitic particles. Figure S1 (Supporting Information) shows SEM images of UFG obtained from the 5, 10, and 20 mg/mL solutions, illustrating the presence of both larger graphitic particles and exfoliated sheets. Size distribution histograms are shown in Figure S2 (Supporting Information), and the relevant statistics are summarized in Table S4. The graphitic particles range in lateral dimensions from a few hundred nanometers to tens of micrometers. On the basis of AFM analysis, smaller

particles are around 9–16 nm in thickness. Cross-sectional views of the larger graphitic particles indicate thicknesses of  $2.5 \pm 2.1 \mu\text{m}$ . At lower loadings of graphite, the smaller particles constitute a greater proportion of the suspended solids, as illustrated by Table S4. These high-solid-loading NMP dispersions allow for preparation of UFG/polyamic acid formulations that yield pinhole-free continuous films upon spray-coating while limiting the amount of NMP that has to be used within the formulations.

Raman spectroscopy data collected for the larger graphitic platelets and thinner exfoliated sheets from 5, 10, and 20 mg/mL UFG dispersions are shown in Figure S3 (Supporting Information). The vertical dashed lines demarcate the positions of the D-band at  $\sim 1350 \text{ cm}^{-1}$ , G-band at  $\sim 1580 \text{ cm}^{-1}$ , and 2D band at  $\sim 2700 \text{ cm}^{-1}$ .<sup>49</sup> The position of the G-band indicates that the recovered materials are few-layered graphene. The thinner exfoliated sheets show prominent D-bands as a result of edge effects.

Figure 1 schematically illustrates the preparation of UFG/polyamic acid nanocomposites and their casting onto abraded AA7075 substrates whereupon imidization is accomplished *in situ* through thermal annealing to obtain the UFG/PEI nanocomposite coating. The stochastic inclusion of *m*-phenylenediamine units within polyamic acid inhibits crystallization and thus yields an amorphous, pliant, and formable polymer matrix. The excellent dispersion of UFG within polyamic acid has been extensively characterized in our previous work<sup>11,18,36</sup> and is facilitated by the *in situ* synthesis of the polymer around the exfoliated graphite platelets;  $\pi$ – $\pi$  interactions of the basal planes of the exfoliated graphite framework with the conjugated anhydride result in the growing polymer framework encasing the filler UFG nanoplatelets.

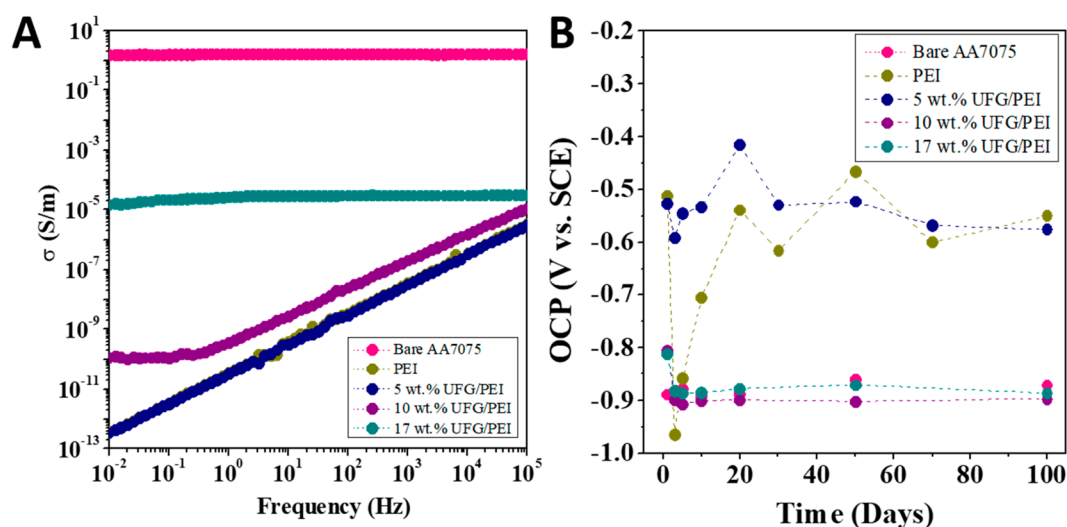


**Figure 2.** (A) AC conductivity measurements of bare AA7075, PEI coated onto AA7075, and UFG/PEI coatings on AA7075 with different UFG loadings and (B) evolution of the OCP for UFG/PEI coatings, PEI-coated AA7075, and bare AA7075 immersed in an aerated aqueous solution of 3.5 wt % NaCl for 100 days at room temperature.

UFG/polyamic acid formulations have been prepared with 5, 10, and 17 wt % UFG loadings, which as delineated in Figure 1 correspond to two different regimes (*vide infra*): the 5 wt % UFG/PEI sample corresponds to well-dispersed UFG below the percolation threshold, where physical isolation of UFG flakes is maintained and the coatings provide tortuous and extended pathways for diffusion of corrodant species through the polymeric network, whereas the 10 and 17 wt % UFG/PEI samples correspond to stabilization of continuous percolative, conductive networks across the polymer matrix. The connectivity of exfoliated graphite inclusions within the coating has a profound influence on the activation of galvanic corrosion mechanisms as will be discussed in subsequent sections, providing a tortuous pathway inhibiting the diffusion of corrodant species at low loadings but activating galvanic corrosion at high loadings when the percolation threshold is reached.

Figure S4 (Supporting Information) shows optical microscopy images of the coated AA7075 surfaces. The inclusion of increasing amounts of UFG in the coatings brings about in a decrease in transparency of the coatings. The 5 and 10 wt % UFG/PEI coatings show similar dispersion, whereas in the 17 wt % UFG/PEI coating, some larger graphitic agglomerates are observed to segregate at the surfaces. Figure S5 (Supporting Information) shows the same coatings at lower magnifications. Figure S6 (Supporting Information) shows SEM images of cryo-fractured 10 wt % UFG/PEI nanocomposite coatings (Figure S6A–D) demonstrating homogeneous dispersion of the UFG inclusions without evidence for local charging indicative of phase segregation; Figure S6E–H furthermore exhibit transmission electron microscopy (TEM) images of 10 wt % UFG/PEI films cast onto a copper grid. The UFG inclusions can be distinguished based on their greater electron density contrast. Figure S6E and F demonstrate the large distribution of sizes of the exfoliated graphite platelets present within the nanocomposite coatings. Larger sheets can be imaged at lower magnifications (Figure S6E), whereas the smaller sheets are observed only at higher magnifications (Figure S6F). The electron microscopy images attest to the excellent dispersion of the graphitic platelets within the polymeric matrix. Further support for the homogeneous

dispersion of UFG inclusions within the coatings comes from cross-sectional SEM images that will be discussed below before and after salt water immersion.

Figure 2 shows AC conductivity data acquired as a function of frequency for bare AA7075, a PEI-coated AA7075 substrate, and exfoliated graphite/PEI-coated substrates with different UFG loadings. The conductivity of the as-prepared exfoliated graphite was similarly measured for drop cast films and is shown for comparison in Figure S7 (Supporting Information). The evolution of AC conductivity in terms of frequency is reflective of the overall electrical conductivity of the composite and is strongly dependent on the extent of dispersion and the dimensions of the conductive filler; as such, it is commonly used to probe the percolation threshold for conductive fillers embedded within dielectric matrices.<sup>50–57</sup> On the basis of evolution of the AC conductivity in terms of frequency, composite coatings containing conductive particles can be categorized in three classes.<sup>50</sup> Below the percolation threshold, the composite material behaves as a dielectric, with the AC conductivity linearly increasing as a function of the frequency. In proximity to the percolation threshold, the AC conductivity is independent of the frequency up to a certain characteristic frequency value. Beyond this point, the AC conductivity again linearly increases as a function of the frequency. Finally, above the percolation threshold, the AC conductivity remains constant across the entire frequency range. In Figure 2, bare AA7075 not surprisingly behaves as a conductive material (as do the exfoliated graphite films in Figure S7), whereas the PEI coating shows characteristic dielectric behavior with an AC conductivity that increases linearly as a function of the frequency. The AC conductivity response of the 5 wt % UFG/PEI coating is essentially the same as that of the pristine PEI coating, which suggests that the exfoliated graphite content in this coating is below the percolation threshold of the material. Interestingly, when the concentration of UFG is increased to 10 wt %, the AC conductivity shows a strongly frequency dependent response with a linear variation of the conductivity as a function of frequency above  $\sim 0.3$  Hz but a frequency-invariant response below this value. In other words, a 10 wt % loading of UFG brings the composite close to its percolative threshold. The 17 wt % UFG/PEI composite shows a

**Table 1.** Summary of Adhesion Testing and Mechanical Properties Measured for PEI and UFG/PEI Nanocomposite Coatings on AA7075

sample	ASTM D4541–09 (pull off)	ASTM D3359 (tape)	ASTM D2197–13 (scrape)	nanoindentation	
	average pull-off pressure (MPa)			elastic modulus (GPa)	hardness (MPa)
PEI	0.73 ± 0.02	5B	>10 kg	5.17 ± 0.10	422 ± 15
5 wt % UFG/PEI	0.76 ± 0.13			4.92 ± 0.32	401 ± 20
10 wt % UFG/PEI	0.77 ± 0.07			4.45 ± 0.30	395 ± 10
17 wt % UFG/PEI	0.67 ± 0.10			5.44 ± 0.31	463 ± 30

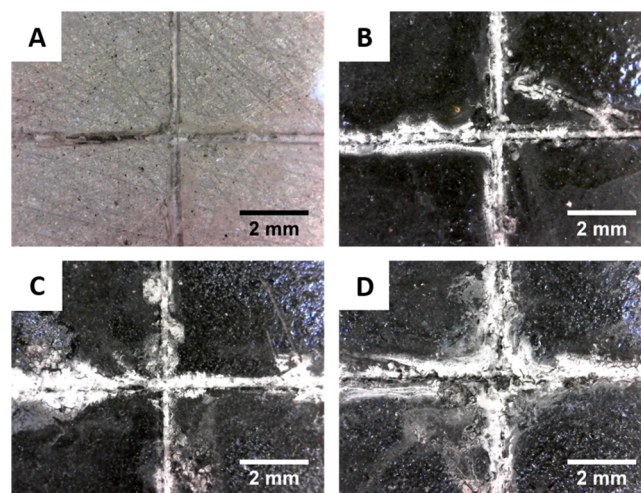
frequency-invariant response characteristic of metallic materials suggesting that the percolation threshold has been reached and that the exfoliated graphite flakes form a continuous electrical network within the polymeric matrix. The data in Figure 2 thus underpin the delineation of the distinctive regimes schematically illustrated in Figure 1, which as described below strongly influences the corrosion performance of these nanocomposite coatings.

Adhesion testing has been performed on each type of coating using ASTM testing procedures (Table 1). Evaluation of the coatings by ASTM D3359, the cross-cut test, shows excellent adhesion of the PEI and UFG/PEI nanocomposite coatings to the abraded AA7075 substrates with all of the coatings earning a rating of 5B, corresponding to no measurable loss of the coating upon peeling of the adhesive tape. Additionally, the ASTM D2197–13 scrape test shows no break in the coatings at the maximum loading of 10 kg. Pull-off testing has also been performed as per ASTM D4541–09. The point of failure for all coatings is the contact between the coating and metal; pull-off pressures for each of the coatings are listed in Table 1. These results demonstrate that the adhesive properties are dominated by the interfacial bonding between PEI and the abraded AA7075 substrate and are not substantially altered by inclusion of UFG.

In contrast, the mechanical properties measured by nanoindentation indicate that the addition of exfoliated graphite indeed influences the elastic and plastic properties of the resulting nanocomposite. As seen in Table 1, the elastic modulus of PEI has been measured to be 5.17 GPa, which is similar to the 2.775 GPa value reported by Khatam and Ravi-Chandar for a PEI strip<sup>58</sup> and the modulus measured using ASTM Standard D638 for PEI resin.<sup>59</sup> Interestingly, in the nanocomposite coating, the addition of exfoliated graphite first leads to a decrease in the elastic modulus and hardness. However, with increasing exfoliated graphite incorporation, the elastic modulus and hardness are substantially increased, surpassing that of the host matrix. The observed non-monotonic behavior highlights the complex mechanical interaction between the exfoliated graphite and PEI. At low UFG loadings, the exfoliated graphite inclusions disrupt cross-linking of the polyamic acid chains resulting in a polymeric matrix that is softer than the host matrix alone. However, at higher UFG loadings, the rule of mixtures prevails and the filler brings about an increase in the elastic modulus and hardness of the composite coatings. Values of elastic moduli in Table 1 are averages of the measured moduli from all loading rates for the specified coating. The elastic moduli measured at each specific loading rate for each coating are shown in Figure S8 (Supporting Information).

**Evaluation of Corrosion Protection Endowed by Nanocomposite Coatings.** As an initial qualitative means of evaluating the corrosion protection afforded to the AA7075 substrates by PEI and UFG/PEI nanocomposite coatings,

coated samples with cross-sectional cuts have been exposed to a salt spray chamber for 12 days. Figure 3 shows digital

**Figure 3.** Digital photographs of the cross-sectional cuts after 12 days of salt spray exposure for (A) PEI-coated AA7075 as well as (B) 5; (C) 10; and (D) 17 wt % UFG/PEI coatings.

photographs of the coatings after 12 days of exposure. The areas at some distance from the cross-sectional cut are unaffected by salt spray exposure, attesting to the excellent barrier properties of the coatings. For the coating comprising just PEI, accumulation of corrosion products is confined to the exposed region of the metal surface. Indeed, the PEI coating functions solely as a barrier, and thus, when the barrier is compromised, corrosion is initiated at the exposed metal surface. In contrast, the UFG/PEI composites show the corrosion product spreading outward from the cross-sectional cut; the amount of the product and the extent of its accumulation scales roughly proportionately to the graphene loading. Creation of a scratch within these coatings allows for contact between the graphene, the electrolyte medium, and the exposed aluminum substrate, thereby establishing a corrosion cell. Given the relative differentials of reduction potentials noted above, exfoliated graphite thus promotes the galvanic corrosion of the AA7075 substrate (Figure 1). Consequently, the mitigation of galvanic couples between conductive exfoliated graphite and the aluminum substrate is imperative to utilize the potential strongly enhanced tortuosity of diffusion pathways accessible upon incorporation of exfoliated graphite.

The evolution of the OCP for the UFG/PEI coatings, PEI coated onto AA7075, and bare AA7075 immersed in a 3.5 wt % aqueous solution of NaCl for 100 days is shown in Figure 2. The bare AA7075 substrate exhibits OCP values close to  $-0.88$  mV versus SCE during the first few days of salt water immersion. These OCP values are associated with active corrosion processes that involve the breakdown of the native

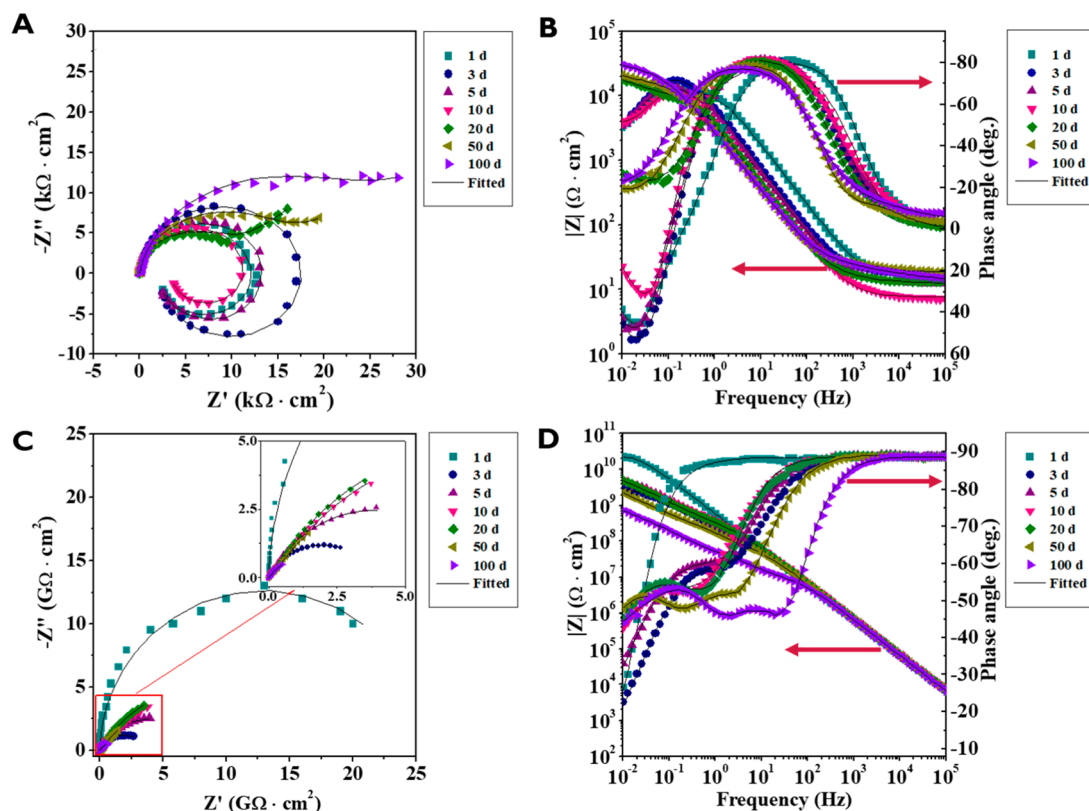


**Figure 4.** EIS spectra monitored for (A, B) AA7075 and (C, D) PEI-coated AA7075 immersed in a 3.5 wt % aqueous solution of NaCl for up to 100 days.

oxide film as a result of attack by reactive  $\text{Cl}^-$  ions in the electrolyte and the initiation of charge transfer processes at the metal/electrolyte interface.<sup>60,61</sup> After about 20 days of immersion, the OCP values of AA7075 are shifted to more anodic values, which suggest the formation of passivating corrosion products at the metal surface that decelerate the corrosion process. In contrast, the measured OCP for the PEI coating is  $-0.50$  V versus SCE for the first day of immersion indicating negligible or absent corrosion processes immediately after immersion. However, the OCP value for the PEI-coated AA7075 substrate is dramatically decreased to more negative values after about 24 h of salt water immersion, approaching values comparable to those measured for bare AA7075. The observed shift can be ascribed to the diffusion of water and ionic species through the coating, which results in the initiation of corrosion processes at the metal/coating interface. However, after 5 days of immersion, the OCP values for PEI are increased to more positive values, which indicated the entrapment of corrosion products underneath the coating, which resulted in the formation of a passivation layer. Indeed, a gradual increase of the OCP values is observed over 20 days of salt water immersion. Subsequently, the OCP values fluctuate between approximately  $-0.45$  and  $-0.60$  V versus SCE. This fluctuation is likely derived from the initiation of pitting corrosion processes wherein pit formation and repassivation occur alternately at active zones on the metal surface. Interestingly, the OCP values for the 5 wt % UFG/PEI coating are suggestive of significantly improved stability against corrosion. As shown in Figure 2, the OCP values remain constant around  $-0.55$  V versus SCE during the entire period of immersion, which indicates that the coating is effective in protecting the metallic substrate from attack by the corrosive

medium and thus corrosion processes are not initiated at the coating/metal interface. However, further addition of graphene to the PEI coating appears to be somewhat detrimental in terms of corrosion inhibition; Figure 2 shows that the OCP values for the 10 and 17 wt % UFG/PEI coatings are slightly more negative as compared to the OCP values for bare AA7075, suggesting greater corrosion activity at the aluminum surface in the presence of relatively high amounts of exfoliated graphite. The values do not increase upon prolonged exposure, which suggests that high amounts of exfoliated graphite inclusions ( $\geq 10$  wt %) accelerate the corrosion process without allowing for formation of an effective passivation layer owing to the formation of galvanic cells.

Electrochemical impedance spectroscopy (EIS) has been used to investigate the evolution of the electrochemical response of the different coatings and the bare AA7075 substrate upon immersion in a 3.5 wt % aqueous solution of NaCl for up to 100 days. Figure 4 plots Nyquist and Bode representations of EIS data measured for bare AA7075 and PEI-coated AA7075 at different immersion times. In Figure 4A, it can be seen that during the first 10 days of immersion, the Nyquist plot for the bare AA7075 substrate is characterized by a capacitive loop from high to intermediate frequencies, which is related to the charge transfer processes at the metal/electrolyte interface; an inductive loop is furthermore observed at the low frequencies and is associated with adsorbed intermediate species (charge transfer process) present during the breakdown of the passivating film and the initiation of pitting corrosion.<sup>62,63</sup> These features can also be identified in the phase angle plot shown in Figure 4B where the capacitive response corresponds to the region from  $10^3$  to  $10^{-1}$  Hz and is characterized by a negative peak value, whereas the inductive

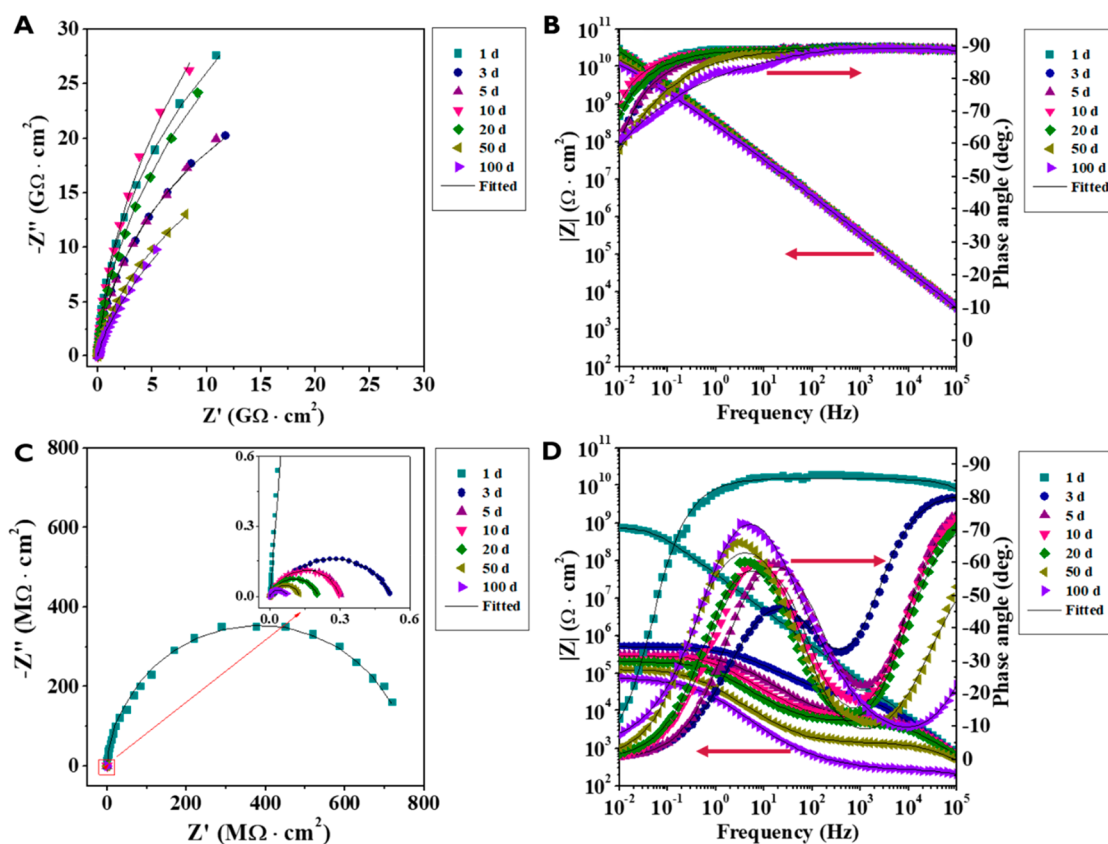


**Figure 5.** EIS spectra monitored for (A, B) 5 wt % UFG/PEI and (C, D) 10 wt % UFG/PEI on AA7075 immersed in a 3.5 wt % aqueous solution of NaCl for up to 100 days.

response is observed at the lowest frequencies and exhibits a positive peak value. After 20 days of immersion, the Nyquist representation (Figure 4A) shows that the inductive loop at low frequencies is no longer present and a diffusion tail is instead observed in this frequency range. The appearance of this feature at low frequencies is indicative of a diffusion-controlled corrosion process such that the formation of corrosion products at the metal/electrolyte interface is limited by the diffusion of reacting species toward and away from the metal surface. The appearance of the diffusion tail after 20 days of immersion is consistent with the increase of the OCP to more positive values at this time (Figure 2) and indicates that the corrosion products formed at the surface are somewhat passivating and can modestly impede the corrosion process and limit charge transfer.

EIS data for the PEI-coated AA7075 substrate are shown in Figure 4C. The Nyquist representation exhibits a large capacitive loop during the first day of immersion covering the entire measured frequency range; such an extended loop derives from the dielectric properties of the organic coating and its resistance to the diffusion of water and ionic species. Notably, the magnitude of the impedance at the lowest frequency ( $|Z|_{0.01 \text{ Hz}}$ ) approaches a value higher than  $10^{10} \Omega \text{ cm}^2$ . Since  $|Z|_{0.01 \text{ Hz}}$  provides an estimation of the effective resistance of the coating system, the high value suggests that the PEI coating provides good barrier protection against aggressive species immediately upon immersion. However, a stark change is observed within 24 h; the  $|Z|_{0.01 \text{ Hz}}$  value is decreased by almost one order of magnitude upon salt water immersion for 3 days. Furthermore, the phase angle plot shows that after 3 days of immersion, a second time constant at a

lower frequency of about 0.4 Hz is observed, which can be ascribed to the initiation of pitting corrosion at the metal/coating interface. Indeed, these data are consistent with the drastic decrease of the OCP value at this immersion time shown in Figure 2. However, upon prolonged immersion, the  $|Z|_{0.01 \text{ Hz}}$  value in Figure 4D as well as the radii of the semicircle in the Nyquist plot of Figure 4C are monotonically increased up until 20 days of immersion as a result of the formation and growth of corrosion products at active sites. These corrosion products are entrapped within the PEI coating and impede the migration of ionic species from and toward the incipient pits formed on the substrate. In other words, the local accumulation of corrosion products at the pit sites delay further propagation of the pit.<sup>64</sup> Further exposure to the electrolyte solution brings about a continuous decrease of  $|Z|_{0.01 \text{ Hz}}$  which reaches a value  $<10^9 \Omega \text{ cm}^2$  at 100 days when the immersion test is concluded. In addition, a third time constant at intermediate frequencies (ca. 0.1–25 Hz) can be distinguished after 50 days of immersion. This response can be attributed to the accumulation of corrosion products at the pit sites. As the corrosion products build up at the pit sites, internal tensile stresses start to develop at the coating/metal interface. These internal stresses weaken the adhesion between the metal and the coating, resulting eventually in local delamination of the coating at the active sites.<sup>64</sup> The continuing partial delamination of the coating from the metal substrate underpins the overall reduction in the corrosion resistance of the system as a function of time.

Figure 5A and B plot EIS data acquired for AA7075 substrates with a 5 wt % UFG/PEI coating. A singular time constant is observed during the entire immersion time. In

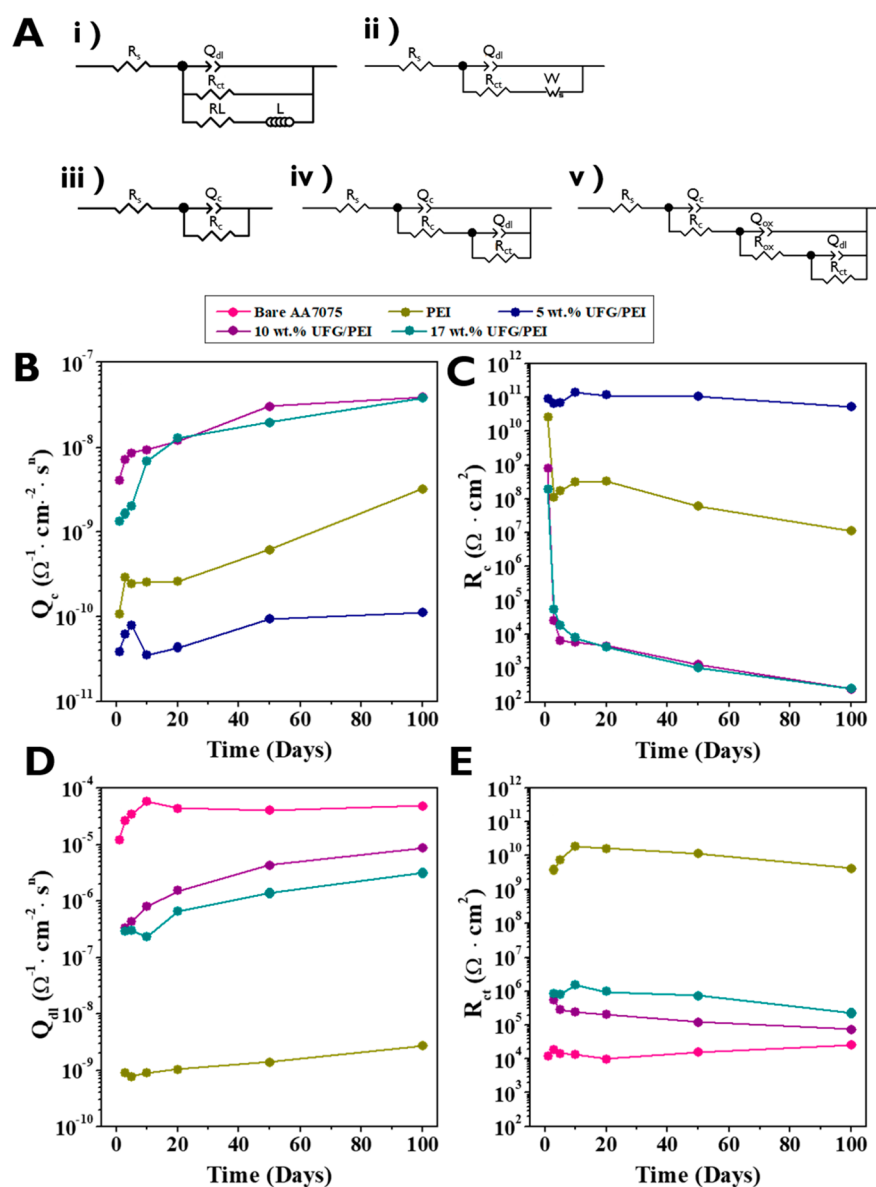


**Figure 6.** (A) Equivalent electrical circuits used to model the EIS response for bare AA7075, PEI, and UFG/PEI coatings immersed in a 3.5 wt % aqueous solution of NaCl for 100 days. Evolution of equivalent circuit elements derived from fitting of EIS spectra of AA7075 and exfoliated graphite/PEI coatings; (B) coating capacitance ( $Q_c$ ), (C) coating resistance ( $R_c$ ), (D) double layer capacitance ( $Q_{dl}$ ), and (E) charge-transfer resistance ( $R_{ct}$ ).

addition, the EIS signal shows an almost ideal capacitive behavior with  $|Z|_{0.01 \text{ Hz}}$  values ranging between  $\sim 3 \times 10^{10} \Omega \text{ cm}^2$  for the first day of immersion to  $1.1 \times 10^{10} \Omega \text{ cm}^2$  upon 100 days of salt water immersion. The slight decrease of  $|Z|_{0.01 \text{ Hz}}$  values corresponds to the slow diffusion of water and ionic species, which have to navigate a path made much more tortuous by the inclusion of graphene, into the coating. Indeed, the results suggest that the 5 wt % UFG/PEI coating shows excellent barrier protection without any signatures of corrosion processes being operational at the coating/metal interface over the entire duration of the testing period. The substantial enhancement in the barrier properties of the nanocomposite as compared to PEI alone can be ascribed to several reasons. At these loadings (below percolation as per Figure 2), 2D sheets of few-layered graphene serve as excellent water-impermeable<sup>27</sup> and ion-impermeable inclusions and greatly reduce the concentration of microscopic defects and pores within the

polymeric matrix. As such, the exfoliated graphite inclusions substantially increase the effective pathlengths for the diffusion of water and chloride ions toward the metal surface.<sup>32,41,65,66</sup> The increase in tortuosity is reflected in a substantially enhanced pore transport resistance. The strong interaction between the  $\pi$ -conjugated basal planes of exfoliated graphite and the aromatic groups of PEI further ensures excellent adhesion without development of porosity at the filler/matrix interface as is often the case with less compatible fillers. The high elastic modulus of graphene and the strong interfacial adhesion ensures that the composite as a whole are able to withstand strains developed during local corrosion without delamination (Figure S8).<sup>36,41</sup>

Figure S3C and D plot analogous EIS data acquired for an AA7075 substrate coated with 10 wt % UFG/PEI. Figure S9 (Supporting Information) shows corresponding data measured for the 17 wt % UFG/PEI coating. Interestingly, the excellent

corrosion inhibition of UFG/PEI nanocomposites at low concentrations of exfoliated graphite is severely compromised when the exfoliated graphite concentration is increased above the percolation threshold. During the first day of salt water immersion, the EIS signal for both coatings is characterized by a singular time constant (Figures S5D and S9B) suggesting that similar to the 5 wt % UFG/PEI sample, no corrosion processes are occurring at the metal/coating interface. However, the  $|Z|_{0.01 \text{ Hz}}$  values for the 10 and 17 wt % UFG/PEI coatings (Figures S5D and S9B) are approximately one and two orders of magnitude lower than that of the 5 wt % UFG/PEI coating (Figure 5B), which connotes decreased efficacy of barrier protection upon increased graphene incorporation. Upon 3 days of salt water immersion, a drastic decrease of the  $|Z|_{0.01 \text{ Hz}}$  values is observed for both the coatings with high loadings of exfoliated graphite, decreasing to values  $<10^6 \Omega \text{ cm}^2$ . Furthermore, Figures S5D and S9B indicate the appearance of another time constant in the range between intermediate and low frequencies ( $10^2 \text{ Hz}$  to  $10^{-1} \text{ Hz}$ ), which is ascribed to the initiation of corrosion processes at the coating/metal interface. This latter behavior persists until the end of the exposure period and along with the successive diminution of  $|Z|_{0.01 \text{ Hz}}$  values with prolonged immersion suggests that the corrosion process proceeds under charge transfer control during the entire time period. It is additionally worth noting that the EIS data for these two coatings do not show the diffusion tail observed for bare AA7075 or the third time constant observed for the PEI coating that are indicative of the accumulation of corrosion products at the metal surface. Instead, it appears that electrochemical activity proceeds for the entire 100 days and the 10 and 17 wt % UFG/PEI coatings promote continuous dissolution of the corrosion products without formation of a passivation layer. The aggressive corrosion observed in the presence of these coatings above percolation threshold can be ascribed to galvanic coupling established between exfoliated graphite and the metal substrate.<sup>22,67–69</sup> Since graphite has a substantially more positive corrosion potential (+0.150 V)<sup>19</sup> as compared to AA7075-T6 (−0.765 V),<sup>20</sup> cathodic reactions are likely to occur at the exfoliated graphite, whereas anodic dissolution reactions are anticipated for the Al alloy substrates when the two are electrochemically coupled. The establishment of a percolative exfoliated graphite network renders the underlying aluminum substrate particularly vulnerable to galvanic corrosion since local oxidative processes at specific pit sites can then be balanced by reductive processes at exfoliated graphite sites located at a substantial distance from the coating/metal interface within the bulk of the coating. Furthermore, the incipient corrosion products are unable to achieve local passivation since the substrate is coupled to an extended exfoliated graphite network and as such corrosion continues unabated as oxidized  $\text{Al}^{3+}$  species can traverse through the film and be reduced at the surfaces of exfoliated graphite particles. Such corrosion acceleration as a result of galvanic coupling has been observed for bare graphene films and is strongly dependent on the electrical conductivity of the exfoliated graphite coating and its ease of degradation such as to form a corrosion cell.<sup>22,33,66,70</sup>

To provide a more quantitative perspective of the performance of the coatings, the equivalent electrical circuits (EECs) sketched in Figure 6A have been used to fit the EIS data plotted in Figures 4 and 5. Table S5 summarizes which of the equivalent circuits shown in Figure 6A have been used to model the EIS over specific time intervals across the duration

of exposure. The equivalent circuit shown in Figure 6A(i) has been used to model the EIS response for bare AA7075 over the first 10 days of salt water immersion. In this circuit,  $R_s$  corresponds to the electrolyte resistance;  $Q_{dl}$  and  $R_{ct}$  denote the double layer capacitance and the charge transfer resistance, respectively, of the pitting corrosion process taking place at the aluminum surface; and  $R_L$  and  $L$  represent the resistance and the inductance, respectively, associated with adsorption of intermediate species at the metal surface during the initiation of the pitting corrosion process.<sup>62</sup> For longer immersion times, beyond 20 days of salt water immersion, the inductance response is no longer observed and thus a Warburg impedance ( $W$ ) component is added to describe the diffusion-controlled process derived from the accumulation of corrosion products at the metal surface (Figure 6A(ii)). The EIS response for the pristine PEI coating has been fitted using the equivalent circuits sketched in Figure 6A(iii)–(v); circuit (iii) has been used for the first day of immersion, circuit (iv) for 3–20 days of immersion, and circuit (v) for 50–100 days of immersion (Table S5). In these circuit diagrams,  $Q_c$  and  $R_c$  represent the capacitance and resistance of the pristine PEI coating, respectively;  $Q_{dl}$  and  $R_{ct}$  represent the double layer capacitance and charge transfer resistance, respectively, as delineated above for bare AA7075; and  $Q_{ox}$  and  $R_{ox}$  describe the capacitance and the resistance, respectively, of the corrosion products that are locally accumulated at the coating/electrolyte interface (and bring about local stresses and delamination as discussed above). The equivalent circuit in Figure 6A(iii) suffices to fit the EIS response of the 5 wt % UFG/PEI coating for the entire immersion time since no corrosion processes are operational at the metal/electrolyte interface, and only modest diffusion of water and ionic species within the polymeric matrix is observed. Circuits (iii) and (iv) have been used to fit the EIS response measured for 10 and 17 wt % UFG/PEI coatings; only the former is necessary for the first day of immersion, whereas the latter captures the continuing corrosion for the remaining duration of salt water immersion. For all the equivalent circuits diagrammed in Figure 6, constant phase elements (CPE) have been used instead of capacitances to take into consideration deviations from ideal capacitive behavior.<sup>71,72</sup> The impedance of the CPE is defined as

$$Z_Q = \frac{1}{Y_0(j\omega)^n} \quad (4)$$

where  $Y_0$  is the admittance of the constant phase element,  $j$  is an imaginary number,  $\omega$  is the frequency, and  $n$  is an empirical exponent in the range between 0 to 1;  $n = 0$  corresponds to a resistor, whereas  $n = 1$  describes a purely capacitive element.<sup>72,73</sup>

Modeling the EIS response of the different coatings using the equivalent circuits noted above allows for systematic comparison of the magnitude of individual elements as a function of the immersion time. Figure 6B plots the time evolution of the coating capacitance ( $Q_c$ ), which is related to the dielectric properties of the coatings and is a measure of the efficacy of barrier protection that the coatings provide against permeation of water and ionic species. Figure 6B indicates that the 5 wt % UFG/PEI coating exhibits the lowest capacitance values of all of the samples, almost an order of magnitude lower than PEI, during the entire immersion time, thereby indicating that it provides the best barrier protection against diffusion of water and ionic species. In addition, the  $Q_c$  values remain most constant across the 100 days of salt water

immersion with only a slight increase suggestive of some permeation of the electrolyte within the coating. In contrast, the  $Q_c$  values for the PEI coating without exfoliated graphite initially increase during the first 5 days of immersion as a result of water uptake (water permeation is substantially increased in the absence of exfoliated graphite) by the coating. The  $Q_c$  value remain essentially constant up to 20 days, suggestive of water saturation. However, after 20 days of immersion, a substantial increase of the  $Q_c$  value is observed and can be related to the local delamination of the coating as noted above. The  $Q_c$  values for 10 and 17 wt % UFG/PEI coatings are significantly higher as compared to the 5 wt % UFG/PEI and PEI coatings, suggesting that high concentrations of exfoliated graphite compromise the barrier properties of the polymeric matrix, likely by forming phase segregated domains (Figure S4). For these coatings, the  $Q_c$  value again shows a rapid increase over the first 10 days of salt water immersion, followed by a slower increase at longer immersion times. The observed progression suggests rapid diffusion of the electrolyte during the early stages of salt water immersion and continuous deterioration of the coating upon prolonged immersion.

The evolution of the coating resistance ( $R_c$ ), shown in Figure 6C, is furthermore concordant with the trends observed for  $Q_c$  values of the different coatings. Figure 6C shows that the 5 wt % UFG/PEI coating has the highest resistance value with  $R_c$  approaching  $10^{11} \Omega \text{ cm}^2$  and holding fairly constant over the entire immersion time. The PEI coating without exfoliated graphite also has a high  $R_c$  value for the first day of immersion (ca.  $3 \times 10^{10} \Omega \text{ cm}^2$ ); however, this value rapidly plummets by over two orders of magnitude as a result of the diffusion of electrolyte, which increases the electrical conductivity of the coating and eventually results in delamination of the coating from the metal surface. The  $R_c$  values for the 10 and 17 wt % UFG/PEI coatings during the first day of immersion are significantly lower as compared to the 5 wt % UFG/PEI coating (ca.  $8 \times 10^8$  and  $2 \times 10^8 \Omega \text{ cm}^2$ , respectively). A drastic decrease of  $R_c$  by almost five orders of magnitude is observed upon prolonged immersion of these higher exfoliated-graphite-content substrates in salt water.

The  $Q_{dl}$  and  $R_{ct}$  circuit elements delineated in Figure 6A (i, ii and iv, v) are related to the charge transfer process at the coating/metal interface. No such process is observed for 5 wt % UFG/PEI.  $Q_{dl}$  is associated with the distribution of ionic charges at the metal/coating interface and is proportional to the electrochemically active area at the interface.<sup>74</sup> Bare AA7075 shows the highest  $Q_{dl}$  values, which reflects current leakage and the high accessible surface area for activation of corrosion processes in the absence of a protective coating. For the PEI-coated sample, relatively small and constant  $Q_{dl}$  values are observed upon initial immersion (Figure 6D). However, these values are increased upon 50 days of immersion as a result of the delamination of the coating from the metal substrate, which exposes a larger area for subsequent corrosive attack. The  $Q_{dl}$  values for 10 and 17 wt % UFG/PEI coatings are more than two orders of magnitude higher than the corresponding values for the PEI coating (Figure 6D). The significant enhancement in electrochemically active sites is suggestive of the operation of galvanic corrosion processes, which accelerate the anodic dissolution of the aluminum substrate. Notably, the  $Q_{dl}$  values continuously increase as a function of the immersion time, which supports the notion stated above that as a result of the galvanically coupled corrosion, a passivating layer of solid corrosion products is not

formed at the metal/coating interface. The charge transfer resistance ( $R_{ct}$ ) values plotted in Figure 6E are in good agreement with the  $Q_{dl}$  trends for the different coatings. PEI exhibits the highest charge transfer resistance, which increases during the first few days of immersion owing to the accumulation of corrosion products at the pit sites, and subsequently decreases as a result of delamination of the coating from the substrate. The evolution of  $R_{ct}$  for the 10 and 17 wt % UFG/PEI coatings corroborate the proposed galvanically accelerated active corrosion hypothesis noted above with no evidence for an increase of charge transfer resistance anticipated when a passivating layer is formed at the coating/metal interface. Taken together, analysis of impedance data acquired over 100 days of salt water exposure provides unprecedented mechanistic insight into the corrosion protection/acceleration endowed by UFG/PEI coatings to aluminum substrates. Below the percolation threshold, the exfoliated graphite inclusions provide substantially increased tortuosity of diffusion pathways and yield an excellent barrier film that protects the aluminum substrate from attack by ionic species. In contrast, PEI without graphene is much more susceptible to permeation of water and ionic species. Remarkably, above the percolation threshold, continuous charge-transfer-controlled electrochemical activity continues to occur at the electrolyte/metal interface and corrosion proceeds without stabilization of the interfacial passivating layer observed for bare AA7075.

The inhibition efficiency (%IE) is often calculated to determine the relative decrease in corrosion rate provided by different coatings in comparison to the corrosion rate for a specified baseline and can be calculated using the following expression:<sup>75,76</sup>

$$\%IE = \left( \frac{R_p - R_p^0}{R_p} \right) \times 100 \quad (5)$$

where  $R_p$  and  $R_p^0$  are the polarization resistances for the coating under consideration and the baseline coating, respectively. The higher the value of  $R_p$ , the greater the effectiveness of the coating in mitigating corrosion processes at the metal substrate.  $R_p$  has been defined as the impedance value at 0 Hz ( $Z_{\omega 0} = R_s - R_p \approx R_p$ ) that describes the total corrosion resistance of the system.<sup>77,78</sup> Following this definition, the  $R_p$  and  $R_p^0$  values can be calculated as follows:

$$\frac{1}{R_p^0} = \frac{1}{R_{ct}^0} + \frac{1}{R_L^0} \rightarrow R_p^0 = \frac{R_{ct}^0 \times R_L^0}{R_{ct}^0 + R_L^0} \quad (6)$$

$$\frac{1}{R_p} = \frac{1}{R_c} \rightarrow R_p = R_c \quad (7)$$

where  $R_c$  is the resistance of the coating,  $R_{ct}^0$  is the charge transfer resistance of the aluminum substrate, and  $R_L^0$  is the resistance associated with the adsorption of intermediate species on bare aluminum. These values have been calculated based on the equivalent circuits shown in Figure 6A. Polarization resistance values for each coating and bare AA7075 at each time point are plotted in Figure S10A. By examining the polarization resistance values alone, substantial differences in performance for each of the coatings can be distinguished. The 5 wt % UFG/PEI coating retains the highest corrosion resistance across the duration of the study with PEI in second place with an order of magnitude lower  $R_p$ .

The values for polarization resistance for the 10 and 17 wt % UFG/PEI coatings are consistently lower as compared to the baseline PEI coating. Additionally, the polarization resistance rapidly decreases for the 10 and 17 wt % UFG/PEI coatings going from being around one to being five orders of magnitude lower than observed for the PEI coating. Using AA7075 as a baseline for comparison (i.e., as  $R_p^0$ ), an inhibition efficiency of 99.99% was maintained for the 5 wt % coating over the course of the 100 days immersion in a 3.5 wt % aqueous solution of NaCl. Using the polarization resistance of PEI as  $R_p^0$ , we have calculated the inhibition efficiency derived from the incorporation of exfoliated graphite particles below the percolation threshold. The evolution of inhibition efficiency with PEI taken to be  $R_p^0$  is plotted for the 5 wt % UFG/PEI coating in Figure S10B as a function of time. Even with respect to PEI, the addition of UFG brings about a substantial improvement. The relative inhibition efficiency starts out low since unmodified PEI acts as a good barrier coating during the initial 24 h; a substantial enhancement of the inhibition efficiency is observed with time and illustrates the role of UFG in increase tortuosity of ion and water transport, whereas PEI alone progressively deteriorates and is delaminated owing to the accumulation of corrosion products. No meaningful numbers for corrosion efficiency can be derived for the 10 and 17 wt % UFG/PEI coatings given the activation of galvanic corrosion, which causes these coatings to have a lower polarization resistance value as compared to PEI.

Figure 7 shows cross-sectional SEM images of the aluminum/coating interface for the PEI coating and 5, 10, and 17 wt % UFG/PEI coatings before and after 100 days of immersion in salt water. The labels in the figure indicate the interfaces and materials being imaged in each case. Figure S11 (Supporting Information) shows additional cross-sectional SEM images of the aluminum/coating interface for the exposed surfaces shown in Figure 7B, D, F, and H at lower magnifications demonstrating that the features shown in Figure 7 are representative for each sample. The PEI coating shows accumulation of corrosion products at the interface as well as notable delamination as surmised above from the observed modulation of the OCP (Figure 2) and  $Q_c$  circuit element values (Figure 6). As discussed above, preferential deposition of corrosion product at the most active sites can give rise to inhomogeneous stress at the interface, which results in localized delamination of the coating. Consistent with the electrochemical characterization discussed above, the 5 wt % UFG/PEI coating is essentially unchanged following salt water exposure without any discernible delamination or accumulation of corrosion product across the entire cross-sectional area. Figure S12 provides additional images of the 5 wt % UFG/PEI coating following immersion in 3.5 wt % NaCl at three separate locations across the interfaces further demonstrating that the coating integrity remains uncompromised over this time period. In stark contrast, the 10 and 17 wt % UFG/PEI coatings show signs of corrosion of the aluminum as well as the accumulation of corrosion product at the surface of the coating. Figure 8 exhibits Al compositional maps acquired across the interfaces for the four coated samples using EDS. While the Al-signal is localized at the substrate for the 5 wt % UFG/PEI coating, diffusion of Al species across the polymer with deposition on the coating surface is observed for the 10 and 17 wt % UFG/PEI coatings. This observation is consistent with the mechanism proposed above wherein as a result of galvanic coupling of aluminum to the percolative graphene

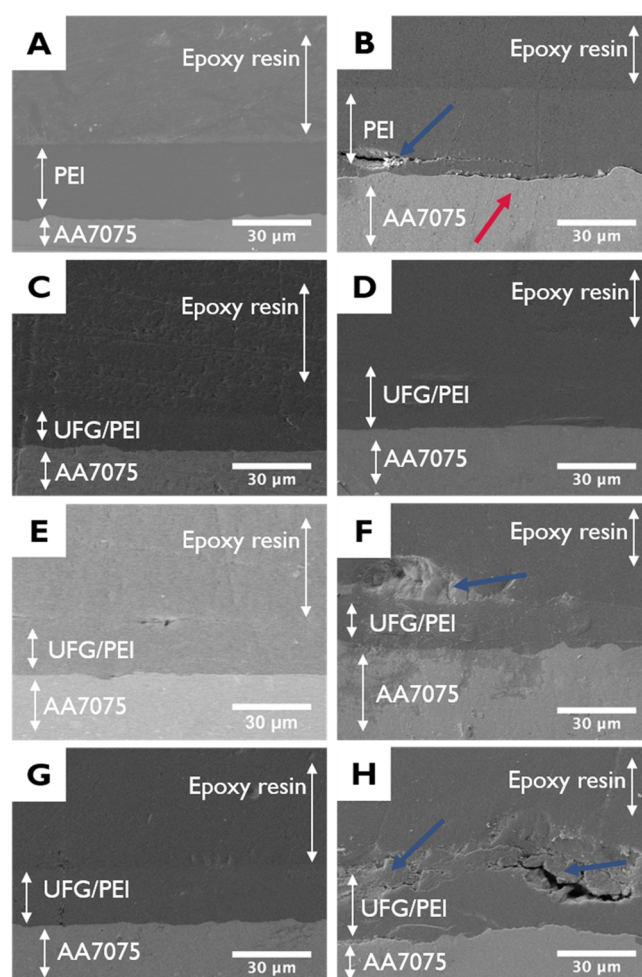


**Figure 7.** Cross-sectional SEM images of coatings on AA7075: (A, B) PEI; (C, D) 5 wt % UFG/PEI; (E, F) 10 wt % UFG/PEI; and (G, H) 17 wt % UFG/PEI coatings shown before and after exposure to a 3.5 wt % aqueous solution of NaCl for 100 days. The red arrow in B delineates a delaminated region and blue arrows indicate regions with corrosion product. The AA7075 substrate, UFG/PEI nanocomposite coating, corrosion product, and epoxy resin used to section the samples can be distinguished.

network, cathodic reduction of  $Al^{3+}$  species can occur throughout the exfoliated graphene network or sparingly soluble oxidized aluminum species can be deposited onto the coating surface.

An idealized model has been developed to evaluate the influence of embedding conductive particles of varying dimensions within a dielectric matrix and its effect therein in altering the tortuosity. A computational first-order homogenization scheme based on the Finite Element method has been implemented. The employed flake size distributions are given in the Tables S2 and S3 (Supporting Information), and exemplary snapshots of the resulting particle distributions are shown in Figure S13.

Table 2 lists the effective (normalized) diffusivity as a function of mass fraction and size distribution. From Table 2, it is apparent that the size distribution of the inclusions has a significant impact on the effective diffusivity of the considered samples. The use of uniformly sized particles results in the diffusivity being nearly unchanged between the 5 and 10 wt % samples. This is due to the fact that the latter contains nearly twice the amount of particles as compared to the former

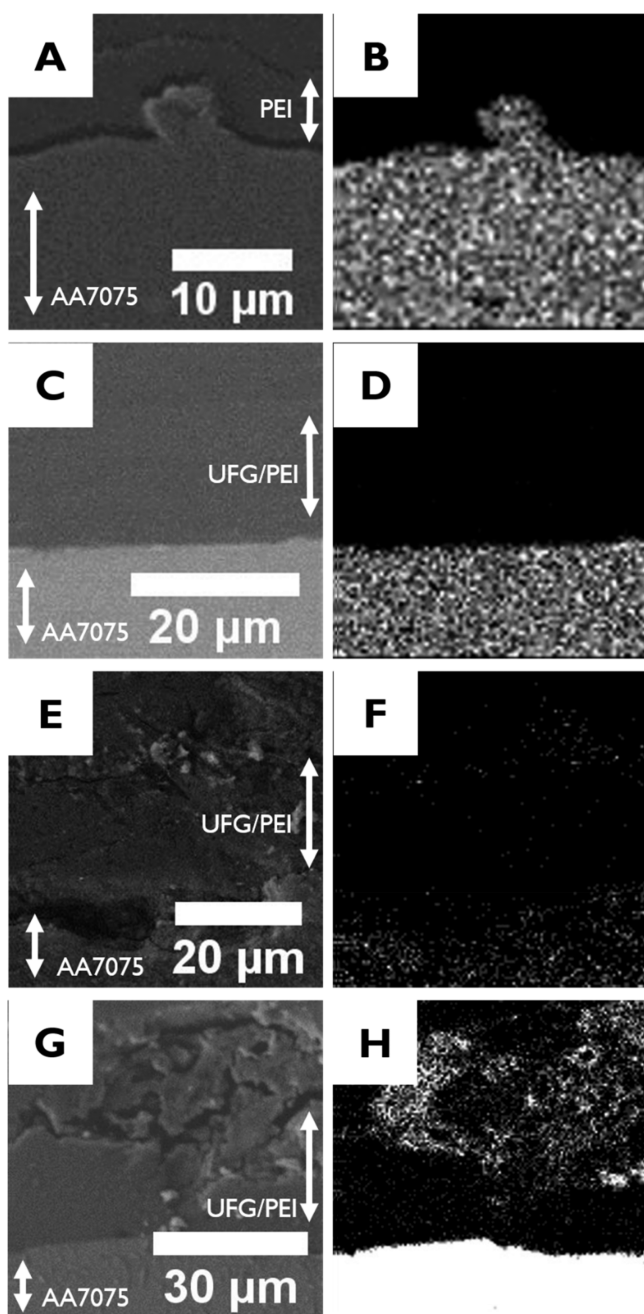


**Figure 8.** SEM images and corresponding Al elemental distribution maps measured by EDS for each of the coatings exposed to a 3.5 wt % aqueous solution of NaCl for 100 days. (A, B) PEI-coated AA7075; (C, D) 5 wt % UFG/PEI; (E, F) 10 wt % UFG/PEI; (G, H) 17 wt % UFG/PEI.

**Table 2. Effective (Normalized) Diffusivity as a Function of Mass Fraction and Size Distribution (with Standard Deviation)**

weight percent (%)	5	10	17
uniform size	$0.916 \pm 0.004$	$0.920 \pm 0.003$	$0.736 \pm 0.016$
size distribution	$0.894 \pm 0.021$	$0.785 \pm 0.053$	$0.705 \pm 0.077$

specimen, albeit with a slightly smaller particle size. Comparing these data with the results calculated from the heterogeneous particle size distributions, it is clear that a pronounced decrease in diffusivity (and hence an increase in tortuosity) is observed

for nonuniform particle size distributions in this range of particle loadings. On the basis of these observations, the use of a heterogeneous particle size distribution is greatly favorable for enhancing the tortuosity and hence the corrosion resistance imparted by a PEI/UFG coating.

## CONCLUSIONS

In summary, exfoliated graphite/PEI coatings have been examined for their ability to inhibit the corrosion of an aerospace alloy, AA7075, as a function of the exfoliated graphite loading upon protracted exposure to saline environments. Two distinct regimes are distinguished: at low exfoliated graphite loadings, below the percolation threshold, the composite coatings endow long-term corrosion protection as a result of the substantially enhanced barrier properties realized by inclusion and dispersion of exfoliated graphite within the polymeric matrix. In contrast, at high exfoliated graphite loadings, above the percolation threshold, the large differential in redox potentials of the AA7075 substrate and the exfoliated graphite network result in galvanic corrosion of the former (Figure 1). A loading of 5 wt % exfoliated graphite within PEI provides excellent corrosion resistance for aluminum AA7075 surfaces with a  $|Z|_{0.01 \text{ Hz}}$  maintained in the range of  $1.1\text{--}3 \times 10^{10} \Omega \text{ cm}^2$  over the course of 100 days of submersion in a 3.5 wt % aqueous solution of NaCl. Constituting the polymeric matrix around the dispersed graphene platelets and the strong  $\pi\text{--}\pi$  interactions between the basal planes of exfoliated graphite and the aromatic rings of the anhydride precursor ensures a dense nanocomposite with excellent dispersion of the filler. The exfoliated graphite inclusions greatly increase the tortuosity of water permeation and ion diffusion pathways from the surface to the substrate as compared to a PEI film of comparable thickness that does not include exfoliated graphite. The latter unmodified polymeric film does endow some corrosion protection by trapping corrosion products at the interface but is nevertheless prone to delamination and continued corrosion. The presence of a broad distribution of exfoliated graphite particle sizes is shown by finite element modeling to endow increased tortuosity and thereby enhanced ion transport resistance.

When the exfoliated graphite loading is above the threshold value needed to achieve percolation, the challenges with corrosion protection of electropositive metals are manifested in full measure. Indeed, loadings of 10 and 17 wt % exfoliated graphite in PEI accelerate corrosion as a result of pronounced differential in redox potentials. Oxidation at the substrate,  $\text{Al}^{3+}$  diffusion, and deposition across the exfoliated graphite network and at the surface is observed without stabilization of a passivating interfacial layer. Such coatings with percolative networks of exfoliated graphite could potentially be used for anodic protection upon application of a voltage. Detailed impedance studies allow for evaluation of capacitance and resistance elements across 100 days of salt water exposure corroborating the distinctive mechanisms observed as a function of exfoliated graphite platelet loadings. The materials developed here thus provide an excellent addition to the sparse repertoire of composites that are viable for the protection of engineered aluminum alloys. Future work will focus on inclusion of electroactive layers such as surface-passivated Mg nanoparticles to additionally impart cathodic protection<sup>12,13</sup> as well as application of recently developed omniphobic composite coatings to limit fluid interactions.<sup>79</sup>

## ■ ASSOCIATED CONTENT

### 📄 Supporting Information

The Supporting Information is available free of charge on the ACS Publications website at DOI: 10.1021/acsanm.9b00451.

AA7075 chemical composition, UFG particle size distributions, Raman spectra of UFG solutions, optical microscopy images of coating surfaces, cryo-fracture SEM images, TEM images, AC conductivities of UFG solutions, nanoindentation results at different loading rates, EIS data of 17 wt % UFG/PEI coatings monitored across 100 days, additional cross-sectional SEM images of coating-metal interfaces, finite element modeling of diffusivity (PDF)

## ■ AUTHOR INFORMATION

### Corresponding Authors

\*E-mail: banerjee@chem.tamu.edu.

\*E-mail: hcastaneda@tamu.edu.

### ORCID

Sarbajit Banerjee: 0000-0002-2028-4675

### Author Contributions

†R.D.D. and Y.C.G. contributed equally to this work.

### Notes

The authors declare no competing financial interest.

## ■ ACKNOWLEDGMENTS

R.D.D. would like to acknowledge the support of the Data-Enabled Discovery and Design of Energy Materials (D3EM) program funded through NSF Award No. DGE-1545403. C.D.F. acknowledges the support of the National Science Foundation Graduate Research Fellowship under Grant No. 1746932. Authors acknowledge the TAMU Materials Characterization Facility (MCF) for work done with SEM and EDS.

## ■ REFERENCES

- (1) Kim, H. C.; Wallington, T. J. Life-Cycle Energy and Greenhouse Gas Emission Benefits of Lightweighting in Automobiles: Review and Harmonization. *Environ. Sci. Technol.* **2013**, *47* (12), 6089–6097.
- (2) Kim, H. C.; Wallington, T. J.; Sullivan, J. L.; Keoleian, G. A. Life Cycle Assessment of Vehicle Lightweighting: Novel Mathematical Methods to Estimate Use-Phase Fuel Consumption. *Environ. Sci. Technol.* **2015**, *49* (16), 10209–10216.
- (3) Luk, J. M.; Kim, H. C.; De Kleine, R.; Wallington, T. J.; MacLean, H. L. Review of the Fuel Saving, Life Cycle GHG Emission, and Ownership Cost Impacts of Lightweighting Vehicles with Different Powertrains. *Environ. Sci. Technol.* **2017**, *51* (15), 8215–8228.
- (4) Mayyas, A.; Qattawi, A.; Omar, M.; Shan, D. Design for Sustainability in Automotive Industry: A Comprehensive Review. *Renewable Sustainable Energy Rev.* **2012**, *16* (4), 1845–1862.
- (5) Ellingsen, L. A. W.; Hung, C. R.; Majeau-Bettez, G.; Singh, B.; Chen, Z.; Whittingham, M. S.; Strömman, A. H. Nanotechnology for Environmentally Sustainable Electromobility. *Nat. Nanotechnol.* **2016**, *11* (12), 1039–1051.
- (6) Huang, R.; Riddle, M.; Graziano, D.; Warren, J.; Das, S.; Nimbalkar, S.; Cresko, J.; Masanet, E. Energy and Emissions Saving Potential of Additive Manufacturing: The Case of Lightweight Aircraft Components. *J. Cleaner Prod.* **2016**, *135*, 1559–1570.
- (7) Long, R. S.; Boettcher, E.; Crawford, D. Current and Future Uses of Aluminum in the Automotive Industry. *JOM* **2017**, *69* (12), 2635–2639.
- (8) Dursun, T.; Soutis, C. Recent Developments in Advanced Aircraft Aluminium Alloys. *Mater. Eng.* **2014**, *56*, 862–871.

- (9) Hughes, A. E.; Cole, I. S.; Muster, T. H.; Varley, R. J. Designing Green, Self-Healing Coatings for Metal Protection. *NPG Asia Mater.* **2010**, *2* (4), 143–151.

- (10) Bibber, J. W. Chromium-Free Conversion Coatings for Zinc and Its Alloys. *J. Appl. Surf. Finish.* **2007**, *2* (4), 273–275.

- (11) Dennis, R. V.; Patil, V.; Andrews, J. L.; Aldinger, J. P.; Yadav, G. D.; Banerjee, S. Hybrid Nanostructured Coatings for Corrosion Protection of Base Metals: A Sustainability Perspective. *Mater. Res. Express* **2015**, *2* (3), 032001.

- (12) Bierwagen, G.; Brown, R.; Battocchi, D.; Hayes, S. Active Metal-Based Corrosion Protective Coating Systems for Aircraft Requiring No-Chromate Pretreatment. *Prog. Org. Coat.* **2010**, *67* (2), 195–208.

- (13) Dennis, R. V.; Viyanalage, L. T.; Aldinger, J. P.; Rout, T. K.; Banerjee, S. Nanostructured Magnesium Composite Coatings for Corrosion Protection of Low-Alloy Steels. *Ind. Eng. Chem. Res.* **2014**, *53* (49), 18873–18883.

- (14) Davidson, R. D.; Cubides, Y.; Andrews, J. L.; McLain, C. M.; Castaneda, H.; Banerjee, S. Magnesium Nanocomposite Coatings for Protection of a Lightweight Al Alloy: Modes of Corrosion Protection, Mechanisms of Failure. *Phys. Status Solidi A* **2019**, 1800817.

- (15) Rekha, M. Y.; Kamboj, A.; Srivastava, C. Electrochemical Behavior of SnNi-Graphene Oxide Composite Coatings. *Thin Solid Films* **2018**, *653*, 82–92.

- (16) Rekha, M. Y.; Punith Kumar, M. K.; Srivastava, C. Electrochemical Behaviour of Chromium-Graphene Composite Coating. *RSC Adv.* **2016**, *6* (67), 62083–62090.

- (17) Nguyen, A. T.; Lai, W.-C.; To, B. D.; Nguyen, D. D.; Hsieh, Y.-P.; Hofmann, M.; Kan, H.-C.; Hsu, C.-C. Layer Control of Tubular Graphene for Corrosion Inhibition of Nickel Wires. *ACS Appl. Mater. Interfaces* **2017**, *9* (27), 22911–22917.

- (18) Dennis, R. V.; Fler, N. A.; Davidson, R. D.; Banerjee, S. Graphene Coatings for the Corrosion Protection of Base Metals. In *Graphene Technology: From Laboratory to Fabrication*; Wiley-VCH Verlag GmbH & Co. KGaA: Weinheim, Germany, 2016; pp 155–176.

- (19) Bellucci, F. Galvanic Corrosion between Nonmetallic Composites and Metals: I Effect of Metal and of Temperature. *Corrosion* **1991**, *47* (10), 808–819.

- (20) Burleigh, T. D.; Rennick, R. C.; Bovard, F. S. Corrosion Potential for Aluminum Alloys Measured by ASTM G 69. *Corrosion* **1993**, *49* (8), 683–685.

- (21) Cui, C.; Lim, A. T. O.; Huang, J. A Cautionary Note on Graphene Anti-Corrosion Coatings. *Nat. Nanotechnol.* **2017**, *12* (9), 834–835.

- (22) Schriver, M.; Regan, W.; Gannett, W. J.; Zaniwski, A. M.; Crommie, M. F.; Zettl, A. Graphene as a Long-Term Metal Oxidation Barrier: Worse Than Nothing. *ACS Nano* **2013**, *7* (7), 5763–5768.

- (23) Lee, J.; Berman, D. Inhibitor or Promoter: Insights on the Corrosion Evolution in a Graphene Protected Surface. *Carbon* **2018**, *126*, 225–231.

- (24) Hsieh, Y.-P.; Hofmann, M.; Chang, K.-W.; Jhu, J. G.; Li, Y.-Y.; Chen, K. Y.; Yang, C. C.; Chang, W.-S.; Chen, L.-C. Complete Corrosion Inhibition through Graphene Defect Passivation. *ACS Nano* **2014**, *8* (1), 443–448.

- (25) Prasai, D.; Tuberquia, J. C.; Harl, R. R.; Jennings, G. K.; Bolotin, K. I. Graphene: Corrosion-Inhibiting Coating. *ACS Nano* **2012**, *6* (2), 1102–1108.

- (26) Schultz, B. J.; Dennis, R. V.; Lee, V.; Banerjee, S. An Electronic Structure Perspective of Graphene Interfaces. *Nanoscale* **2014**, *6* (7), 3444–3466.

- (27) Zhang, D.; Wang, D. Z.-R.; Creswell, R.; Lu, C.; Liou, J.; Herman, I. P. Passivation of CdSe Quantum Dots by Graphene and MoS<sub>2</sub> Monolayer Encapsulation. *Chem. Mater.* **2015**, *27* (14), 5032–5039.

- (28) Sun, W.; Wang, L.; Wu, T.; Wang, M.; Yang, Z.; Pan, Y.; Liu, G. Inhibiting the Corrosion-Promotion Activity of Graphene. *Chem. Mater.* **2015**, *27* (7), 2367–2373.

- (29) Chen, C.; Qiu, S.; Cui, M.; Qin, S.; Yan, G.; Zhao, H.; Wang, L.; Xue, Q. Achieving High Performance Corrosion and Wear Resistant Epoxy Coatings via Incorporation of Noncovalent Functionalized Graphene. *Carbon* **2017**, *114*, 356–366.
- (30) Li, Y.; Yang, Z.; Qiu, H.; Dai, Y.; Zheng, Q.; Li, J.; Yang, J. Self-Aligned Graphene as Anticorrosive Barrier in Waterborne Polyurethane Composite Coatings. *J. Mater. Chem. A* **2014**, *2* (34), 14139–14145.
- (31) Qiu, S.; Li, W.; Zheng, W.; Zhao, H.; Wang, L. Synergistic Effect of Polypyrrole-Intercalated Graphene for Enhanced Corrosion Protection of Aqueous Coating in 3.5% NaCl Solution. *ACS Appl. Mater. Interfaces* **2017**, *9* (39), 34294–34304.
- (32) Gu, L.; Liu, S.; Zhao, H.; Yu, H. Facile Preparation of Water-Dispersible Graphene Sheets Stabilized by Carboxylated Oligoanilines and Their Anticorrosion Coatings. *ACS Appl. Mater. Interfaces* **2015**, *7* (32), 17641–17648.
- (33) Sun, W.; Wang, L.; Wu, T.; Pan, Y.; Liu, G. Synthesis of Low-Electrical-Conductivity Graphene/Pernigraniline Composites and Their Application in Corrosion Protection. *Carbon* **2014**, *79*, 605–614.
- (34) Kim, H.; Abdala, A. A.; Macosko, C. W. Graphene/Polymer Nanocomposites. *Macromolecules* **2010**, *43* (16), 6515–6530.
- (35) Tang, L. C.; Wan, Y. J.; Yan, D.; Pei, Y. B.; Zhao, L.; Li, Y. B.; Wu, L.; Bin Jiang, J. X.; Lai, G. Q. The Effect of Graphene Dispersion on the Mechanical Properties of Graphene/Epoxy Composites. *Carbon* **2013**, *60*, 16–27.
- (36) Dennis, B. R. V.; Viyanalage, L. T.; Anil, V. Graphene Nanocomposite Coatings for Protecting Low-Alloy Steels From Corrosion. *Am. Ceram. Soc. Bull.* **2013**, *92* (5), 18–24.
- (37) Ramezanzadeh, B.; Bahlakeh, G.; Mohamadzadeh Moghadam, M. H.; Mirafteb, R. Impact of Size-Controlled *p*-Phenylenediamine (PPDA)-Functionalized Graphene Oxide Nanosheets on the GO-PPDA/Epoxy Anti-Corrosion, Interfacial Interactions and Mechanical Properties Enhancement: Experimental and Quantum Mechanics Investigations. *Chem. Eng. J.* **2018**, *335*, 737–755.
- (38) Yu, F.; Camilli, L.; Wang, T.; Mackenzie, D. M. A.; Curioni, M.; Akid, R.; Bøggild, P. Complete Long-Term Corrosion Protection with Chemical Vapor Deposited Graphene. *Carbon* **2018**, *132*, 78–84.
- (39) Kim, S.; Le, T.-H. H.; Park, C. S.; Park, G.; Kim, K. H.; Kim, S.; Kwon, O. S.; Lim, G. T.; Yoon, H. A Solution-Processable, Nanostructured, and Conductive Graphene/Polyaniline Hybrid Coating for Metal-Corrosion Protection and Monitoring. *Sci. Rep.* **2017**, *7*, 15184.
- (40) Compton, O. C.; Kim, S.; Pierre, C.; Torkelson, J. M.; Nguyen, S. T. Crumpled Graphene Nanosheets as Highly Effective Barrier Property Enhancers. *Adv. Mater.* **2010**, *22* (42), 4759–4763.
- (41) Upadhyayula, V. K. K.; Meyer, D. E.; Gadhamshetty, V.; Koratkar, N. Screening-Level Life Cycle Assessment of Graphene-Poly(Ether Imide) Coatings Protecting Unalloyed Steel from Severe Atmospheric Corrosion. *ACS Sustainable Chem. Eng.* **2017**, *5* (3), 2656–2667.
- (42) Rout, T. K.; Gaikwad, A. V.; Dingemans, T. A *Method of Preparing a Polyetherimide Coating on a Metallic Substrate*. Patent WO2011035920A1, 2010.
- (43) Oliver, W. C.; Pharr, G. M. An Improved Technique for Determining Hardness and Elastic Modulus Using Load and Displacement Sensing Indentation Experiments. *J. Mater. Res.* **1992**, *7* (06), 1564–1583.
- (44) Sun, D.-M.; Liu, C.; Ren, W.-C.; Cheng, H.-M. A Review of Carbon Nanotube- and Graphene-Based Flexible Thin-Film Transistors. *Small* **2013**, *9* (8), 1188–1205.
- (45) Secor, E. B.; Prabhuramirashi, P. L.; Puntambekar, K.; Geier, M. L.; Hersam, M. C. Inkjet Printing of High Conductivity, Flexible Graphene Patterns. *J. Phys. Chem. Lett.* **2013**, *4* (8), 1347–1351.
- (46) Hernandez, Y.; Nicolosi, V.; Lotya, M.; Blighe, F. M.; Sun, Z.; De, S.; McGovern, I. T.; Holland, B.; Byrne, M.; Gun'ko, Y. K.; et al. High-Yield Production of Graphene by Liquid-Phase Exfoliation of Graphite. *Nat. Nanotechnol.* **2008**, *3* (9), 563–568.
- (47) De Jesus, L. R.; Dennis, R. V.; Depner, S. W.; Jaye, C.; Fischer, D. A.; Banerjee, S. Inside and Outside: X-Ray Absorption Spectroscopy Mapping of Chemical Domains in Graphene Oxide. *J. Phys. Chem. Lett.* **2013**, *4* (18), 3144–3151.
- (48) You, Y.; Sahajwalla, V.; Yoshimura, M.; Joshi, R. K. Graphene and Graphene Oxide for Desalination. *Nanoscale* **2016**, *8* (1), 117–119.
- (49) Ferrari, A. C.; Meyer, J. C.; Scardaci, V.; Casiraghi, C.; Lazzeri, M.; Mauri, F.; Piscanec, S.; Jiang, D.; Novoselov, K. S.; Roth, S.; Geim, A. K. Raman Spectrum of Graphene and Graphene Layers. *Phys. Rev. Lett.* **2006**, *97*, 187401.
- (50) Kim, Y. J.; Shin, T. S.; Choi, H.; Do Kwon, J. H.; Chung, Y.-C. C.; Yoon, H. G. Electrical Conductivity of Chemically Modified Multiwalled Carbon Nanotube/Epoxy Composites. *Carbon* **2005**, *43* (1), 23–30.
- (51) Fan, P.; Wang, L.; Yang, J.; Chen, F.; Zhong, M. Graphene/Poly(Vinylidene Fluoride) Composites with High Dielectric Constant and Low Percolation Threshold. *Nanotechnology* **2012**, *23* (36), 365702.
- (52) Gardea, F.; Lagoudas, D. C. Characterization of Electrical and Thermal Properties of Carbon Nanotube/Epoxy Composites. *Composites, Part B* **2014**, *56*, 611–620.
- (53) Seidel, G. D.; Bisrat, Y.; Lagoudas, D. C. Electrical and Thermal Conductivities of Carbon Nanotube-Epoxy Composites: Modeling and Characterization In *Vol. 1: Advances in Aerospace Technology*; ASME, 2007; pp 245–253.
- (54) Sandler, J. K. W.; Kirk, J. E.; Kinloch, I. A.; Shaffer, M. S. P.; Windle, A. H. Ultra-Low Electrical Percolation Threshold in Carbon-Nanotube-Epoxy Composites. *Polymer* **2003**, *44* (19), 5893–5899.
- (55) Thakre, P. R.; Bisrat, Y.; Lagoudas, D. C. Electrical and Mechanical Properties of Carbon Nanotube-Epoxy Nanocomposites. *J. Appl. Polym. Sci.* **2010**, *116* (1), 191–202.
- (56) Sandler, J.; Shaffer, M. S.; Prasse, T.; Bauhofer, W.; Schulte, K.; Windle, A. Development of a Dispersion Process for Carbon Nanotubes in an Epoxy Matrix and the Resulting Electrical Properties. *Polymer* **1999**, *40* (21), 5967–5971.
- (57) Li, J.; Ma, P. C.; Chow, W. S.; To, C. K.; Tang, B. Z.; Kim, J. K. Correlations between Percolation Threshold, Dispersion State, and Aspect Ratio of Carbon Nanotubes. *Adv. Funct. Mater.* **2007**, *17* (16), 3207–3215.
- (58) Khatam, H.; Ravi-Chandar, K. On the Evaluation of the Elastic Modulus of Soft Materials Using Beams with Unknown Initial Curvature. *Strain* **2013**, *49* (5), 420–430.
- (59) Mark, J. E. *Polymer Data Handbook*, 2nd ed.; Oxford University Press, 2009.
- (60) Treu, B. L.; Joshi, S.; Pinc, W. R.; O'Keefe, M. J.; Fahrenholtz, W. G. Characterization of Localized Surface States of Al 7075-T6 during Deposition of Cerium-Based Conversion Coatings. *J. Electrochem. Soc.* **2010**, *157* (8), C282–C287.
- (61) Mert, B. D.; Solmaz, R.; Kardaş, G.; Yazıcı, B. Copper/Polypyrrole Multilayer Coating for 7075 Aluminum Alloy Protection. *Prog. Org. Coat.* **2011**, *72* (4), 748–754.
- (62) Aliramezani, R.; Raeissi, K.; Santamaria, M.; Hakimzad, A. Characterization and Properties of PEO Coatings on 7075 Al Alloy Grown in Alkaline Silicate Electrolyte Containing KMnO<sub>4</sub> Additive. *Surf. Coat. Technol.* **2017**, *329*, 250–261.
- (63) Tian, W.; Li, S.; Wang, B.; Liu, J.; Yu, M. Pitting Corrosion of Naturally Aged AA 7075 Aluminum Alloys with Bimodal Grain Size. *Corros. Sci.* **2016**, *113*, 1–16.
- (64) Zhu, D.; Van Ooij, W. J. Corrosion Protection of AA 2024-T3 by Bis-[3-(Triethoxysilyl)Propyl]Tetrasulfide in Sodium Chloride Solution.: Part 2: Mechanism for Corrosion Protection. *Corros. Sci.* **2003**, *45* (10), 2177–2197.
- (65) Chang, C.-H.; Huang, T.-C.; Peng, C.-W.; Yeh, T.-C.; Lu, H.-I.; Hung, W.-I.; Weng, C.-J.; Yang, T.-I.; Yeh, J.-M. Novel Anticorrosion Coatings Prepared from Polyaniline/ Graphene Composites. *Carbon* **2012**, *50*, 5044–5051.

(66) Hu, J.; Ji, Y.; Shi, Y.; Hui, F.; Duan, H.; Lanza, M. A Review on the Use of Graphene as a Protective Coating against Corrosion. *Ann. Mater. Sci. Eng.* **2014**, *1* (3), 1–16.

(67) Hayatdavoudi, H.; Rahsepar, M. A Mechanistic Study of the Enhanced Cathodic Protection Performance of Graphene-Reinforced Zinc Rich Nanocomposite Coating for Corrosion Protection of Carbon Steel Substrate. *J. Alloys Compd.* **2017**, *727*, 1148–1156.

(68) Rashad, M.; Pan, F.; Yu, Z.; Asif, M.; Lin, H.; Pan, R. Investigation on Microstructural, Mechanical and Electrochemical Properties of Aluminum Composites Reinforced with Graphene Nanoplatelets. *Prog. Nat. Sci.* **2015**, *25* (5), 460–470.

(69) Chaudhry, A. U.; Mittal, V.; Mishra, B. Inhibition and Promotion of Electrochemical Reactions by Graphene in Organic Coatings. *RSC Adv.* **2015**, *5* (98), 80365–80368.

(70) Zhou, F.; Li, Z.; Shenoy, G. J.; Li, L.; Liu, H. Enhanced Room-Temperature Corrosion of Copper in the Presence of Graphene. *ACS Nano* **2013**, *7* (8), 6939–6947.

(71) Harb, S. V.; Pulcinelli, S. H.; Santilli, C. V.; Knowles, K. M.; Hammer, P. A Comparative Study on Graphene Oxide and Carbon Nanotube Reinforcement of PMMA-Siloxane-Silica Anticorrosive Coatings. *ACS Appl. Mater. Interfaces* **2016**, *8* (25), 16339–16350.

(72) Trdan, U.; Grum, J. SEM/EDS Characterization of Laser Shock Peening Effect on Localized Corrosion of Al Alloy in a near Natural Chloride Environment. *Corros. Sci.* **2014**, *82*, 328–338.

(73) Zoltowski, P. On the Electrical Capacitance of Interfaces Exhibiting Constant Phase Element Behaviour. *J. Electroanal. Chem.* **1998**, *443*, 149–154.

(74) Pourhashem, S.; Vaezi, M. R.; Rashidi, A.; Bagherzadeh, M. R. Exploring Corrosion Protection Properties of Solvent Based Epoxy-Graphene Oxide Nanocomposite Coatings on Mild Steel. *Corros. Sci.* **2017**, *115*, 78–92.

(75) Iroh, J. O.; Su, W. Corrosion Performance of Polypyrrole Coating Applied to Low Carbon Steel by an Electrochemical Process. *Electrochim. Acta* **2000**, *46* (1), 15–24.

(76) Zhang, G.; Chen, C.; Lu, M.; Chai, C.; Wu, Y. Evaluation of Inhibition Efficiency of an Imidazoline Derivative in CO<sub>2</sub>-Containing Aqueous Solution. *Mater. Chem. Phys.* **2007**, *105* (2–3), 331–340.

(77) Scully, J. R. Polarization Resistance Method for Determination of Instantaneous Corrosion Rates. *Corrosion* **2000**, *56* (2), 199–218.

(78) Qin, S.; Cubides, Y.; Lazar, S.; Ly, R.; Song, Y.; Gerringer, J.; Castaneda, H.; Grunlan, J. C. Ultrathin Transparent Nanobrick Wall Anticorrosion Coatings. *ACS Appl. Nano Mater.* **2018**, *1* (10), 5516–5523.

(79) O'Loughlin, T. E.; Dennis, R. V.; Fleer, N. A.; Alivio, T. E. G.; Ruus, S.; Wood, J.; Gupta, S.; Banerjee, S. Biomimetic Plastronic Surfaces for Handling of Viscous Oil. *Energy Fuels* **2017**, *31* (9), 9337–9344.